

Non-Gaussian mechanical entanglement with nonlinear optomechanics: generation and verification

Lydia A. Kanari-Naish,^{1,*} Jack Clarke,¹ Sofia Qvarfort,^{1,2} and Michael R. Vanner^{1,†}

¹*QOLS, Blackett Laboratory, Imperial College London, London SW7 2BW, United Kingdom*

²*Department of Physics and Astronomy, University College London, London WC1E 6BT, United Kingdom*

(Dated: Latest revision: November 15, 2021)

Cavity quantum optomechanics has emerged as a new platform for quantum science and technology and has applications ranging from quantum-information processing to tests of the foundations of physics. Of crucial importance for optomechanics is the generation and verification of non-Gaussian states of motion and a key outstanding challenge is the observation of a canonical two-mode Schrödinger-cat state in the displacement of two mechanical oscillators. In this work, we introduce a protocol that utilizes the nonlinearity of the radiation-pressure interaction combined with photon-counting measurements to generate this bipartite non-Gaussian mechanical state. Our protocol employs short optical pulses to both generate the mechanical quantum state, and to then measure arbitrary mechanical quadrature moments, which we utilize to verify the non-Gaussian entanglement. Our entanglement-verification procedure can be used to evaluate an entire class of inseparability criteria and also provides a route for experimental characterisation of a broad range of single- and multi-partite mechanical states. Key experimental factors, such as optical loss and mechanical decoherence, are carefully analyzed and we show that the scheme is feasible with only minor improvements to current experiments that operate outside the resolved-sideband regime. Our scheme provides a new avenue for quantum experiments with entangled mechanical oscillators and offers significant potential for further research and development that utilizes such non-Gaussian states for quantum-information and sensing applications, and for studying the quantum-to-classical transition.

I. INTRODUCTION

Quantum mechanics allows for two or more objects to exhibit correlations that are stronger than is permitted by classical physics. Such quantum correlations are one of the most counter-intuitive and powerful aspects of quantum mechanics, and offer exciting routes for quantum technologies and fundamental physics. Indeed, sufficiently strong correlations, i.e. quantum entanglement, provide significant potential to surpass limitations set by classical physics for widespread applications, including quantum communications [1], computing [2, 3], networking [4, 5], and sensing [6, 7]. Additionally, entanglement is central to many studies of fundamental physics with a prominent example being tests of Bell nonlocality [8–10].

With cavity quantum optomechanics now providing a rapidly progressing new platform for quantum science [11], quantum entanglement in macroscopic mechanical oscillators is currently emerging as an active avenue of study. In particular, the radiation-pressure optomechanical interaction can be utilized to generate a rich variety of different entangled states. Notably, this interaction, when linearized, gives rise to Gaussian entanglement between optical and mechanical modes, which has been studied both theoretically and experimentally. Theoretically, entanglement between both field and mechanics, and also between two mechanical elements has been explored in this regime [12–19]. While experimen-

tally, two-mode squeezed states have been prepared between a microwave field and a mechanical oscillator [20], and continuous-variable entanglement between two mechanical oscillators has also been generated [21–23]. In addition to such Gaussian states, the linearized regime combined with photon-counting enables the preparation of single- and two-mode non-Gaussian mechanical states [24–27]. Recent experimental progress using this combination has enabled single-phonon addition and subtraction to single-mode mechanical systems [28–34], and, similarly, to generate two-mode spatially-separated entangled mechanical oscillators [35, 36]. Furthermore, photon-counting protocols have been proposed to create macroscopic superposition states which can help to overcome the challenge of single-photon weak coupling [37, 38]. Beyond the linearized regime, continued experimental progress has enabled early signatures of the intrinsically cubic radiation-pressure interaction to be observed [39, 40], and there has also been increasing theoretical interest in this nonlinear regime [41–45]. Owing to the importance of nonlinearities in quantum science and technology, bi- and multi-partite quantum state preparation in the nonlinear regime and the subsequent verification of the resulting non-Gaussian entangled states is of key interest. Theoretical progress in this direction has examined entangling operations and the properties of the states generated [46–48], and this nonlinear regime remains as a rich avenue for mechanical quantum-state preparation. Crucially, an experimental recipe for mechanical continuous-variable non-Gaussian entanglement verification remains outstanding.

In this work, we propose how to generate two-mode

* l.kanari-naish18@imperial.ac.uk

† m.vanner@imperial.ac.uk (www.qmeas.net)

mechanical Schrödinger-cat states encoded in the displacement of two mechanical oscillators, and importantly introduce an operational technique to verify the non-Gaussian entanglement with a new scheme to measure arbitrary mechanical moments. Our protocol consists of two separate stages, both utilizing pulsed optomechanical interactions [49] in the unresolved sideband regime to provide a quantum-non-demolition-type interaction with the mechanical position quadrature. For entanglement generation in the first stage, we take advantage of the nonlinear radiation-pressure interaction together with photon-counting measurements with an interferometric set-up to herald a two-mode mechanical Schrödinger-cat state. For the second stage, where we wish to verify the entanglement, we propose a method to determine arbitrary mechanical moments utilizing subsequent pulsed measurements with an iterative verification protocol whereby lower-order moments are used to unlock higher-order moments. We then use the moments obtained to evaluate inseparability criteria which identify the presence of non-Gaussian entanglement [50].

Our scheme is applicable to present-day experiments and non-Gaussian entanglement can be created and verified with only minor improvements to current experiments operating outside the resolved sideband regime. To establish the feasibility of this scheme, we carefully model the key experimental factors including decoherence of the mechanical state within the timescale of the verification stage; and optical losses, detection inefficiency, and dark counts in the heralding stage. The specific form of the non-Gaussian mechanical entanglement generated by our scheme has a wide range of applications with prominent examples including quantum metrology [7], quantum teleportation [51], and fault-tolerant quantum computation [52]. More broadly, these entangled states can also be applied for empirical studies of quantum macroscopicity [53, 54], sensing, and the quantum-to-classical transition [55–58].

II. ENTANGLEMENT PROTOCOL

We first outline our scheme to generate non-Gaussian entanglement between two mechanical oscillators before exploring each stage in more detail. This entanglement scheme can be applied to optomechanical systems that operate outside the resolved sideband regime $\kappa \gg \omega_M$ (where κ is the cavity amplitude decay rate and ω_M is the mechanical angular frequency). We consider two distinct configurations involving a Mach-Zehnder interferometer set-up: (i) the ‘parallel’ case where light in the two paths interact with separate mechanical oscillators (see Fig. 1a), and (ii) the ‘series’ case where only light in the first path interacts with two mechanical oscillators sequentially (see Fig. 1b). In both cases, a pulse of light is first injected into one input of the interferometer. The light in the lower interferometer-path is subjected to a phase shift ϕ , which is an experimental handle that

allows us to directly influence the the properties of the resulting mechanical quantum states. Following a pulsed nonlinear optomechanical interaction [59–61], the two optical modes recombine at another 50:50 beam splitter and are subsequently measured by photon-counting detectors. We denote the event where m and n photons are detected in the two outputs as $\{m, n\}$ thus heralding the creation of the entangled mechanical state $\rho_{\text{out}}^{\{m, n\}}$.

We consider separately two initial optical states to implement our scheme. Firstly, a weak coherent state, i.e. $|\Phi\rangle_L = |\alpha\rangle_1 |0\rangle_2$, where subscripts 1 and 2 denote upper and lower light modes in the interferometer. And, secondly, a single-photon input, i.e. $|\Phi\rangle_L = |1\rangle_1 |0\rangle_2$ which offers advantages for the quantum measurement process, however with the increased experimental complexity of requiring a single-photon source. At the first beam splitter the light interacts with the vacuum mode and undergoes the following transformations: $U_{12}^\dagger a_1 U_{12} \rightarrow (a_1 + a_2)/\sqrt{2}$ and $U_{12}^\dagger a_2 U_{12} \rightarrow (a_1 - a_2)/\sqrt{2}$, where a_1 and a_2 are the annihilation operators associated with modes 1 and 2. The subsequent interaction between the optical pulse and the mechanical oscillator is captured by the following Hamiltonian:

$$H_{\text{int}} = -\hbar g_0 a_i^\dagger a_i (b_j + b_j^\dagger), \quad (1)$$

where g_0 is the optomechanical coupling rate, and b_j is the mechanical annihilation operator for the j^{th} oscillator. We assume the same g_0 for the two optomechanical cavities for brevity and clarity of presentation, but that can be readily generalized if needed. In this pulsed regime, the pulse duration is much shorter than the mechanical period allowing us to model the optomechanical interaction by the unitary $e^{i\mu a_i^\dagger a_i X_{M_j}}$; where $\mu \propto g_0/\kappa$ is the dimensionless coupling strength (and depends on the shape of the pulse), and $X_{M_j} = (b_j + b_j^\dagger)/\sqrt{2}$ is the position-quadrature operator of the j^{th} mechanical system.

An $\{m, n\}$ click heralds the mechanical state $\rho_{\text{out}}^{\{m, n\}} = \Upsilon_{mn} \rho_{\text{in}} \Upsilon_{mn}^\dagger / P_{mn}$, where ρ_{in} is the initial mechanical density operator, and P_{mn} is the probability of an $\{m, n\}$ click event. The measurement operator Υ_{mn} captures the propagation of the light through the interferometer, its interaction with the mechanical systems, and the final measurement of $\{m, n\}$ photons. For the parallel configuration, this is given by $\Upsilon_{mn} = \langle m | \langle n | U_{12}^\dagger e^{i\mu a_1^\dagger a_1 X_{M_1}} e^{i\mu a_2^\dagger a_2 X_{M_2}} e^{i\phi a_2^\dagger a_2} U_{12} |\Phi\rangle_L$, where $|m\rangle$ and $|n\rangle$ are Fock states. The measurement operator for the series configuration can be deduced in a similar manner. For $|\Phi\rangle_L = |\alpha\rangle_1 |0\rangle_2$, the measurement operators are:

$$\Upsilon_{mn} = \mathcal{N}_{mn} [e^{i\mu X_{M_1}} + e^{i\mu X_{M_2} + i\phi}]^m [e^{i\mu X_{M_1}} - e^{i\mu X_{M_2} + i\phi}]^n, \quad (2a)$$

$$\Upsilon_{mn} = \mathcal{N}_{mn} [e^{i\mu(X_{M_1} + X_{M_2})} + e^{i\phi}]^m [e^{i\mu(X_{M_1} + X_{M_2})} - e^{i\phi}]^n, \quad (2b)$$

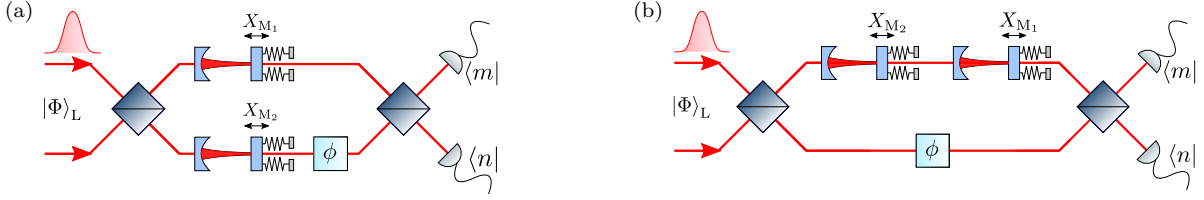


FIG. 1. Proposed experimental schematics to prepare mechanical oscillators in a two-mode Schrödinger-cat state. Both schemes involve injecting a weak coherent state $|\Phi\rangle_L = |\alpha\rangle_1 |0\rangle_2$, or a single photon $|\Phi\rangle_L = |1\rangle_1 |0\rangle_2$ into a Mach-Zehnder interferometer containing two optomechanical cavities. Following a nonlinear interaction, photon-counting is then performed at the two outputs of the interferometer, with counts $\{m, n\}$, that heralds the creation of the mechanical state $\rho_{out}^{\{m,n\}}$. The phase ϕ influences the properties of the state. (a) The ‘parallel’ set-up described by the measurement operator in Eq. (2a). (b) The ‘series’ set-up described by the measurement operator in Eq. (2b). The phase ϕ in both configurations is used to control the properties of the resulting non-Gaussian entangled mechanical state.

for the parallel and series set-ups, respectively. For a single photon input state $|\Phi\rangle_L = |1\rangle_1 |0\rangle_2$, the measurement operators are:

$$\Upsilon_{mn} = \mathcal{N}_{mn} [(e^{i\mu X_{M1}} + e^{i\mu X_{M2} + i\phi}) \delta_{m,1} \delta_{n,0} + (e^{i\mu X_{M1}} - e^{i\mu X_{M2} + i\phi}) \delta_{m,0} \delta_{n,1}], \quad (3a)$$

$$\Upsilon_{mn} = \mathcal{N}_{mn} [(e^{i\mu(X_{M1} + X_{M2})} + e^{i\phi}) \delta_{m,1} \delta_{n,0} + (e^{i\mu(X_{M1} + X_{M2})} - e^{i\phi}) \delta_{m,0} \delta_{n,1}], \quad (3b)$$

for the parallel and series cases, respectively. The prefactor \mathcal{N}_{mn} depends on the injected light state $|\Phi\rangle_L$:

$$\mathcal{N}_{mn} = \begin{cases} e^{-\frac{|\alpha|^2}{2}} \left(\frac{\alpha}{2}\right)^{m+n} \frac{1}{\sqrt{n!m!}} & \text{for } |\Phi\rangle_L = |\alpha\rangle_1 |0\rangle_2, \\ 1/2 & \text{for } |\Phi\rangle_L = |1\rangle_1 |0\rangle_2. \end{cases} \quad (4)$$

Two-mode mechanical Schrödinger-cat states are heralded by the click events $\{1, 0\}$ or $\{0, 1\}$. In fact, the operators Υ_{10} and Υ_{01} can be made identical with a π phase shift in the interferometer. As ϕ is an experimental control, we only need to consider one of these operators to probe the entanglement structure of the state. Therefore, without loss of generality, subsequent analysis will focus on the click event $\{1, 0\}$, which heralds the mechanical state $\rho_{out}^{\{1,0\}}$.

As a motivating example, let us consider the case where the mechanical oscillators are initially in their ground states $\rho_{in} = |0\rangle\langle 0| \otimes |0\rangle\langle 0|$, an optical coherent state is used $|\Phi\rangle_L = |\alpha\rangle_1 |0\rangle_2$, and a $\{1, 0\}$ click event is obtained. For this case, the heralded mechanical states in the parallel and series set-ups, respectively, are given by:

$$|\Psi\rangle_{10} \propto \left(\left| \frac{i\mu}{\sqrt{2}} \right\rangle |0\rangle + e^{i\phi} |0\rangle \left| \frac{i\mu}{\sqrt{2}} \right\rangle \right), \quad (5a)$$

$$|\Psi\rangle_{10} \propto \left(\left| \frac{i\mu}{\sqrt{2}} \right\rangle \left| \frac{i\mu}{\sqrt{2}} \right\rangle + e^{i\phi} |0\rangle |0\rangle \right), \quad (5b)$$

and are independent of which input optical pulse $|\Phi\rangle_L$ is used. The mechanical states in Eqs. 5a and 5b are two-mode Schrödinger-cat states; the state $|i\mu/\sqrt{2}\rangle$ represents a displacement to the ground state and can be un-

derstood as a momentum kick imparted by a single photon. Since $\langle 0|i\mu/\sqrt{2}\rangle = e^{-\mu^2/4}$, for large μ the two components become increasingly orthogonal, and approach maximally-entangled Bell states in the coherent basis. We also note that for $\mu \ll 1$ and with $\phi = \pi$, we can expand Eqs. (5a) and (5b) in the Fock basis. This also results in the Bell states $|\Psi^\pm\rangle = (|0\rangle|1\rangle \pm |1\rangle|0\rangle)/\sqrt{2}$ where $|\Psi^-\rangle$ corresponds to the parallel state in Eq. (5a) and $|\Psi^+\rangle$ the series state in (5b). Indeed, a calculation of the von Neumann entanglement entropy [62] confirms that for a given value of μ the entanglement is optimized when $\phi = \pi$.

We now turn our attention to an initial thermal state $\rho_{in} = \rho_{\bar{n}_1} \otimes \rho_{\bar{n}_2}$, where $\rho_{\bar{n}_j}$ denotes the j^{th} oscillator being in a thermal state with thermal occupation number \bar{n}_j . The resulting state $\rho_{out}^{\{1,0\}}$ approaches the desired two-mode Schrödinger-cat state as \bar{n}_1 and \bar{n}_2 are reduced and the probability of generating $\rho_{out}^{\{1,0\}}$ is:

$$P_{10} = \mathcal{N}_{10} [1 + e^{-\mu^2(1+\bar{n}_1+\bar{n}_2)/2} \cos(\phi)]. \quad (6)$$

With a coherent state input pulse, P_{10} is maximised when $|\alpha| = 1$. We note that the mechanical states produced by the parallel (Fig. 1a) and series schemes (Fig. 1b) are related by a local unitary operation. Acting on the bi-partite mechanical state produced in the parallel set-up with the unitary $D_2(i\mu/\sqrt{2})R_2(\pi)$ will map the state onto the density matrix produced via the series set-up, where $R_2(\pi) = e^{-i\pi b_2^\dagger b_2}$, and $D_2(i\mu/\sqrt{2})$ is a displacement operator acting on oscillator 2. Therefore, the von Neumann entropies of entanglement of the states produced via the parallel and series configurations are identical [63]. Nevertheless, implementing the parallel set-up may be more experimentally convenient as it more easily ensures temporal-mode matching at the beam splitter. Therefore, subsequent analysis will consider the entangled mechanical state produced by the parallel configuration.

III. ENTANGLEMENT VERIFICATION

We propose an experimental procedure in order to measure the components needed to test inseparability criteria for the state produced via the parallel-configuration (Fig. 1a). We include the analogous verification set-up for the series configuration in Appendix A 2. The verification protocol is tailored towards assessing inseparability criteria belonging to the class of criteria in Ref. [50]. These inseparability tests take the form of inequalities (constructed from physical observables) which when violated verify the existence of entanglement. The experimental procedure we propose here can provide access to all the inequalities belonging to this class of inseparability criteria. To demonstrate the strength of our scheme we have selected two such inequalities from this class; one of which is guaranteed to detect entanglement in Gaussian states, while the other is able to detect entanglement in states with a greater degree of non-Gaussianity.

A. Inseparability Criteria

Numerous inseparability criteria have been proposed to study continuous-variable bipartite states, including operational criteria for Gaussian entanglement detection [64–66], and methods for finding optimal continuous-variable entanglement witnesses [67–69]. For a review see Ref. [70]. While the von Neumann entanglement entropy quantifies exactly the bipartite entanglement of pure states, it does not have an operational interpretation when the initial mechanical state ρ_{in} is a mixed ensemble, e.g. a thermal state. Indeed, many continuous-variable entanglement tests are necessary and sufficient for detecting entanglement in Gaussian states, however not all are capable of capturing entanglement in highly non-Gaussian states. While Gaussian states are fully characterised by their first and second moments, the same is not true for a non-Gaussian state [71]. Since higher-order moments are needed to characterise non-Gaussian states, criteria formed from higher-order moments are a natural choice for confirming non-Gaussian entanglement. Shchukin and Vogel introduced a class of inseparability criteria derived from the negative partial transpose (NPT) of the state which take the form of inequalities constructed from arbitrary moments of a continuous-variable quantum state [50]. Therefore, this class of operational criteria lends itself well to the identification of entanglement in non-Gaussian states.

The NPT criterion is a sufficient condition for the entanglement of a quantum state [72, 73], and for continuous-variable bipartite systems, the criterion manifests itself in the negativity of sub-determinants of a matrix constructed in a specific way from observable moments of the state [50]. The determinant calculated from the first N rows and columns of the matrix is denoted as D_N . If $D_N < 0$ for any N then NPT has been demonstrated and the state is entangled. The first few rows and

columns of the matrix from which D_N is calculated are shown here:

$$D_N = \begin{vmatrix} 1 & \langle b_1 \rangle & \langle b_1^\dagger \rangle & \langle b_2 \rangle & \langle b_2 \rangle & \dots \\ \langle b_1^\dagger \rangle & \langle b_1^\dagger b_1 \rangle & \langle b_1^{\dagger 2} \rangle & \langle b_1^\dagger b_2 \rangle & \langle b_1^\dagger b_2 \rangle & \dots \\ \langle b_1 \rangle & \langle b_1^2 \rangle & \langle b_1 b_1^\dagger \rangle & \langle b_1 b_2^\dagger \rangle & \langle b_1 b_2 \rangle & \dots \\ \langle b_2 \rangle & \langle b_1 b_2 \rangle & \langle b_1^\dagger b_2 \rangle & \langle b_2^\dagger b_2 \rangle & \langle b_2^2 \rangle & \dots \\ \langle b_2^\dagger \rangle & \langle b_1 b_2^\dagger \rangle & \langle b_1^\dagger b_2^\dagger \rangle & \langle b_2^{\dagger 2} \rangle & \langle b_2 b_2^\dagger \rangle & \dots \\ \vdots & \vdots & \vdots & \vdots & \vdots & \ddots \end{vmatrix}. \quad (7)$$

Other entanglement criteria are found to exist within this formalism [12, 65, 74, 75]. In particular, D_5 (the determinant of the first 5 rows and columns of the matrix in Eq. (7)) is a reformulation of Simon’s criterion [64] which is a necessary and sufficient entanglement test for single-mode bipartite Gaussian states [76]. Therefore, applying D_5 to a Gaussian state will always verify entanglement (although some non-Gaussian entangled states might also satisfy $D_5 < 0$ since D_5 is only a sufficient condition for non-Gaussian entangled states).

We can construct other inseparability criteria by deleting rows and columns of the matrix in Eq. (7) in a pairwise fashion. If the determinant of the resulting matrix is negative then this also fulfils the NPT criterion and the state is entangled. In this way, we can delete entries in D_N to arrive at the following subdeterminant:

$$S_3 = \begin{vmatrix} 1 & \langle b_2^\dagger \rangle & \langle b_1 b_2^\dagger \rangle \\ \langle b_2 \rangle & \langle b_2^\dagger b_2 \rangle & \langle b_1 b_2^\dagger b_2 \rangle \\ \langle b_1^\dagger b_2 \rangle & \langle b_1^\dagger b_2^\dagger b_2 \rangle & \langle b_1^\dagger b_1 b_2^\dagger b_2 \rangle \end{vmatrix}, \quad (8)$$

such that if $S_3 < 0$ we have a sufficient criterion for entanglement.

Since D_5 captures all entanglement for Gaussian states, if S_3 indicates entanglement in a region of state space for which D_5 does not, we can conclude that these entangled states are non-Gaussian. Therefore, applying these two inequalities together to a state, we can identify parameter regions where the state is non-Gaussian and entangled. We note that there may be entangled non-Gaussian states that are not detected by D_5 or S_3 . Furthermore, for states where both $S_3 < 0$ and $D_5 < 0$, or $D_5 < 0$ but $S_3 > 0$, we cannot infer if the entangled state is non-Gaussian. It should also be highlighted that the magnitude of a determinant has no relevance to the NPT criterion; only the sign of a determinant matters for entanglement verification. Nevertheless, a more negative determinant could be easier to experimentally confirm since each expectation value has an associated experimental uncertainty. We will explore the effect of errors arising from decoherence on the expectation values in Sec. III C.

B. Verification protocol

We now detail our experimental scheme to obtain the moments of the mechanical state which are needed for

the inseparability criteria in Sec. III A. Our verification protocol can be used to extract arbitrary mechanical moments. These can then be used to calculate D_5 and S_3 or more complicated subdeterminants composed of higher-order moments.

The experimental schematic for the verification protocol is illustrated in Fig. 2. Having created the entangled mechanical state using the scheme in Fig. 1a, up to four identical pulses of light are sent into each arm of the apparatus. Assuming the verification pulses are strong and the optical phase shift imparted to the light is small, we get the following linearized optomechanical interaction for each pulse: $U_v = e^{i\chi X_{L_i} X_{M_j}}$, where X_{L_i} and X_{M_j} are the position operators of the i^{th} light mode and j^{th} oscillator respectively [17–19]. The dimensionless interaction strength χ depends on the properties of the input pulse. Note that for the verification pulses to provide an independent readout compared with the entangling pulse, and to operate in the linearized regime, these fields can be resonant with a different optical mode. An additional deterministic momentum kick is also imparted on the system depending on the optical intensity, which may be accounted for in post-processing or cancelled with an appropriate feedback force.

Following the interaction U_v , the i^{th} -mode light quadratures X_{L_i} and P_{L_i} are given by:

$$X_{L_i}(\theta_j) = X_{L_{\text{in}}} \quad (9a)$$

$$P_{L_i}(\theta_j) = P_{L_{\text{in}}} + \chi X_{M_j}(\theta_j), \quad (9b)$$

where $X_{M_j}(\theta_j)$ is the mechanical position operator before the interaction U_v . Here, we have assumed the input light quadratures $X_{L_{\text{in}}}$ and $P_{L_{\text{in}}}$ are quantum noise limited with variances of $1/2$, and the mechanical quadratures freely evolve as a function of $\theta_j = \omega_{M_j} \tau$, where ω_{M_j} is the mechanical frequency of the j^{th} oscillator, and τ is the time elapsed between state generation and the interaction U_v . We henceforth assume that the two oscillators have the same parameters for brevity and drop the j label on ω_M . In the absence of mechanical decoherence $X_{M_j}(\pi/2) = P_{M_j}(0)$, so by switching on the verification pulse at different times we can imprint different mechanical quadratures on P_{L_i} .

As X_M, P_M are more experimentally accessible than b, b^\dagger we will recast the determinants in Eqs. (7) and (8) to be in terms of these operators using the relation $b_i = (X_{M_i} + iP_{M_i})/\sqrt{2}$. From this, each element of D_N (Eq. (7)) can be expressed as a linear combination of moments in X_M and P_M : $\sum_{pqrst} c_{pqrs} \langle X_{M_1}^p P_{M_1}^q X_{M_2}^r P_{M_2}^s \rangle$ where $c_{pqrs} \in \mathbb{C}$. This is convenient as the optomechanical interaction in Eq. (9b) is dependent on the mechanical quadratures.

To obtain all the terms in the inseparability criteria we must measure moments of the form $\langle X_{M_1}^p P_{M_1}^q X_{M_2}^r P_{M_2}^s \rangle$. Since we cannot simultaneously measure X_{M_i} and P_{M_i} , we exploit a network of switches, time delays, and phase shifts $\{\zeta_l\}$ in the optical set-up (Fig. 2) to probe these quantities. This network should be integrated with the

optical apparatus used for entanglement generation as each verification run involves recreating the entangled state. Our proposed scheme allows us to control which combination of mechanical quadratures are obtained via homodyne measurement of the output light quadratures P_{L_k} , where $k = \{A, B, C, D\}$ (see Fig. 2).

We can build up a histogram of P_{L_k} for a particular optical pathway (a specific combination of switches, time-delays, and phase shifts characterises a pathway) by repeatedly generating the mechanical state, and then performing a verification pulse with homodyne detection. From the histogram we can then extract $\langle P_{L_k} \rangle, \langle P_{L_k}^2 \rangle, \dots, \langle P_{L_k}^d \rangle$. Eq. (9b) allows us to expand the measured $\langle P_{L_k}^d \rangle$ as a linear combination of mechanical quadrature moments with coefficients determined by the phase shifts $\{\zeta_l\}$. Repeating these steps with sufficiently many appropriate combinations of $\{\zeta_1, \zeta_2, \zeta_3, \zeta_4\}$ will provide us with enough linearly independent equations to solve for any of the mechanical quadrature moments that appear the expansion of $\langle P_{L_k}^d \rangle$ [77]. From these moments D_5, S_3 , or any other subdeterminant can then be calculated.

As a simple example we can consider finding $\langle X_{M_1} \rangle$. After a $\{1,0\}$ click heralds the state $\rho_{\text{out}}^{\{1,0\}}$, the verification pulses are allowed to interact with the mechanical oscillators. Spectral filters ensure the verification pulses follow a different pathway to that of the entangling pulse, since the entangling and verification pulses have a different wavelength (see Fig. 2). For this mechanical quadrature moment, a single verification pulse is injected at time $\tau = 0$ into the upper arm and interacts with oscillator 1. The pulse then follows path 1b, passes through a set of beam splitters (for this moment $\{\zeta_l\}$ are unimportant). Finally, we perform a homodyne measurement of P_{L_k} (Eq. (9b)). Over numerous runs (each time recreating the entangled state) we build a histogram of P_{L_k} and from its shape deduce the first moment $\langle P_{L_k} \rangle = \chi \langle X_{M_1} \rangle / 2$ (where we have assumed vacuum noise statistics $\langle P_{L_{\text{in}}} \rangle = 0$, and the factor $1/2$ arises from the beam splitters). The value of χ is assumed to be known accurately via an initial calibration stage (see Appendix A 1 c), allowing us to extract the value of $\langle X_{M_1} \rangle$. Repeating this entire sequence but sending in a single pulse at time $\tau = \pi/(2\omega_M)$ will yield $\langle P_{M_1} \rangle$. We can calculate higher-order moments of P_{L_k} from the same histogram. For example, the third moment can be expressed as $\langle P_{L_k}^3 \rangle = \chi^3 \langle X_{M_1}^3 \rangle / 8 + \chi \langle X_{M_1} \rangle / 4$ (where we have assumed $\langle P_{L_{\text{in}}}^3 \rangle = 0$ and $\langle P_{L_{\text{in}}}^2 \rangle = 1/2$). This contains the already-calculated term $\langle X_{M_1} \rangle$, and so we can now determine $\langle X_{M_1}^3 \rangle$. Continuing this iterative procedure, we can use lower-order moments to iteratively find those of higher order.

The full method for finding an arbitrary mechanical moment $\langle X_{M_1}^p P_{M_1}^q X_{M_2}^r P_{M_2}^s \rangle$ is outlined in Appendix A 1 a, while a simpler experimental approach for finding some of the lower-order moments in D_5 and S_3 is presented in Appendix A 1 b. The iterative nature of our verification scheme (using lower-order moments to

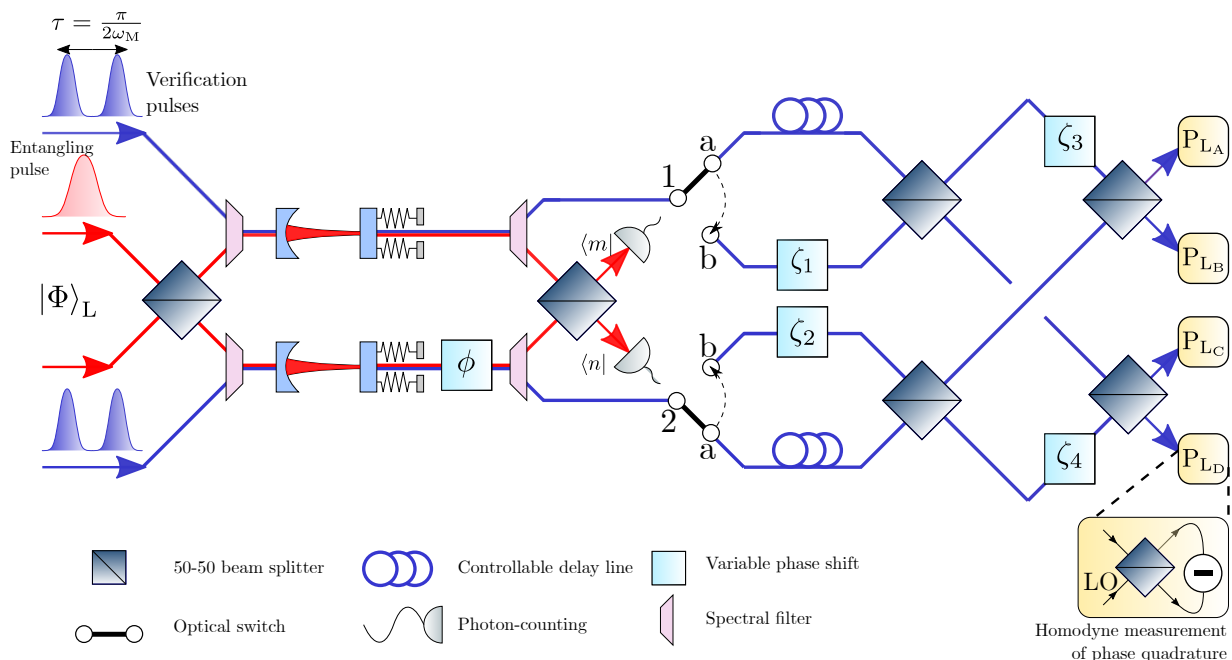


FIG. 2. Proposed verification scheme to measure arbitrary quadrature moments of the mechanical state produced in the parallel configuration. These moments allow us to compute the inseparability criteria D_5 (Eq. (7)) and S_3 (Eq. (8)). The entangling pulse, indicated by the red path on the diagram, generates a mechanical state. Following a $\{1,0\}$ click event, the verification stage is subsequently conducted. Up to 4 pulses of light are sent into apparatus (2 in each arm) at times $\tau = 0$ and/or $\tau = \pi/(2\omega_M)$. These pulses, denoted by the blue path on the diagram, have a different wavelength to the entangling pulse and so spectral filters ensure that the verification and entangling pulses follow different optical paths. Following an optomechanical interaction, the light quadratures of the verification pulse transform according to Eqs. (9a)-(9b); mechanical quadrature information is transferred to the momentum quadrature of light. Switches 1 and 2 provide the option to hold earlier pulses in a delay line, ensuring all pulses are incident at the beam splitters concurrently. Pulses which do not require a delay follow path 1b or 2b. Variable phase shifts ζ_l (where $l = 1, 2, 3, 4$) can be changed between pulses and runs, providing us with the degrees of freedom necessary to solve for the desired moments. Homodyne measurements P_{L_k} (where $k = A, B, C, D$) are performed on the momentum quadrature of light as it emerges from the final set of beam splitters. For each configuration of pulses, switches, and phase shifts, we require many runs (each requiring state creation followed by a measurement of P_{L_k}) in order to construct a histogram of P_{L_k} . From the P_{L_k} distributions one can extract moments such as $\langle P_{L_k}^d \rangle$ which can be expanded in terms of mechanical quadrature moments, thus allowing us to find all moments of the form $\langle X_{M_1}^p P_{M_1}^q X_{M_2}^r P_{M_2}^s \rangle$.

find higher ones) means that, by determining all the moments for S_3 , one also unlocks all the lower-order moments for D_5 , making it experimentally convenient to calculate both determinants together. Unlike pure optical schemes [78], our protocol allows increasingly high-order moments of the bipartite state to be found without requiring additional optical apparatus (only those in Fig. 2).

C. Open-system dynamics

In the verification protocol described in the previous section, we assumed that the mechanical state does not undergo decoherence while the verification stage is performed. This idealised version captures the essence of the scheme; however, we now consider the decoherence that occurs during the time elapsed between state preparation and the verification stage. We henceforth assume that the two oscillators are in identical thermal environ-

ments, and share the same mechanical properties and initial thermal state ($\bar{n}_1 = \bar{n}_2 = \bar{n}$). The mechanical quadratures evolve between X_{M_i} and P_{M_i} and undergo damping and rethermalisation due to their coupling with an external heat bath. This behaviour is described by the following quantum Langevin equations:

$$\dot{X}_{M_i} = \omega_M P_{M_i}, \quad (10a)$$

$$\dot{P}_{M_i} = -\omega_M X_{M_i} - \gamma P_{M_i} + \sqrt{2\gamma}\xi_i, \quad (10b)$$

where γ is the damping rate, and ξ_i is Brownian force term acting on the i^{th} oscillator which models random excitations from the bath. The Brownian force has the following properties:

$$\langle \xi_i(t) \rangle = 0, \quad (11a)$$

$$\langle \xi_i(t)\xi_j(t') \rangle = (2\bar{n}_B + 1)\delta(t-t')\delta_{ij}, \quad (11b)$$

where \bar{n}_B is the thermal occupation number of the bath. In general, $\bar{n} \neq \bar{n}_B$ if cooling strategies are implemented.

The time-dependent solutions to these coupled differential equations are given by Eqs. (B1a)-(B1b) in Appendix B. Mechanical decoherence occurs during the time delays between verification pulses and is characterised by the oscillators' quality factors $Q = \omega_M/\gamma$, and \bar{n}_B .

D. Single-photon detector considerations

With a single photon input state, the use of a $\{1,0\}$ click event to herald the mechanical state $\rho_{\text{out}}^{\{1,0\}}$ is robust against optical losses: if a photon is lost in the interferometer, no click is detected and this run of the experiment is discarded. In contrast, a coherent state input risks creating a mechanical state which is different to that indicated by the photodetector clicks. In Sec. II we noted that when $|\Phi\rangle_L = |\alpha\rangle_1 |0\rangle_2$, choosing $|\alpha| = 1$ maximises the probability of heralding the state $\rho_{\text{out}}^{\{1,0\}}$ (Eq. (6)). However, it is possible that a different mechanical state $\rho_{\text{out}}^{\{m,n\}}$ (where $(m,n) \neq (1,0)$) is created even when the detectors have recorded a $\{1,0\}$ click due to optical losses, detector inefficiencies, or dark counts. We would then incorrectly identify this state as $\rho_{\text{out}}^{\{1,0\}}$, resulting in a 'false positive' event. Conversely, when a $\{1,0\}$ click heralds the successful creation of $\rho_{\text{out}}^{\{1,0\}}$ this is a 'true positive' event. We can model the optical losses and detector inefficiencies by introducing loss-model beam splitters to Figs. 1a and 1b with intensity transmission η (see Fig. 7 in Appendix C) such that when $\eta = 1$ there are no optical losses and the detectors are perfectly efficient. Following the derivation in Appendix C, we demonstrate that when using number-resolving photodetectors, the fraction \mathcal{F} of true positive events per total number of $\{1,0\}$ clicks is expected to be:

$$\mathcal{F} = \left[e^{(1-\eta)|\alpha|^2} + \frac{e^{-\eta|\alpha|^2} \mathcal{D}}{\eta P_{10}(1-\mathcal{D})} \right]^{-1}, \quad (12)$$

where \mathcal{D} is the probability of detecting a single dark count in the detection window, and P_{10} is defined in Eq. (6) (for $|\Phi\rangle_L = |\alpha\rangle_1 |0\rangle_2$). Therefore, provided that $(1-\eta)|\alpha|^2 \ll 1$, and \mathcal{D} is sufficiently low compared to P_{10} , we can neglect false positives and assume that all $\{1,0\}$ clicks truly herald the $\rho_{\text{out}}^{\{1,0\}}$ state. The pulsed regime constrains the detection window to a small enough duration (10 ns considered here using parameters discussed below) such that we can assume \mathcal{D} is on the order of 10^{-8} , and that the probability of multiple dark counts in the window is negligible.

We can derive a similar condition to Eq. (12) for the case of non-resolving detectors which is given by Eq. (C8) in Appendix C. The non-resolving approach similarly requires \mathcal{D} and optical loss to be sufficiently low such that we can neglect false positives. The behaviour of this ratio is further examined in Sec. VB.

IV. RESULTS

In this section we present our results for the verification of entanglement between two optomechanical oscillators which have been prepared in the state $\rho_{\text{out}}^{\{1,0\}}$, using the parallel set-up shown in Fig. 1a. The oscillators are initialized in a separable thermal state ρ_{in} with equal \bar{n} . For a summary of all the experimental parameters see Table I.

Firstly we present our results for the inseparability criteria D_5 (Eq. (7)) and S_3 (Eq. (8)). The moments for these criteria were calculated using the mechanical decoherence model outlined in Sec. III C. This model allows us to simulate the damping and decoherence effects that would arise in an experimental implementation of the verification scheme outlined in Fig. 2. As previously mentioned, we assume that both oscillators are initially identical with the same quality factor Q , thermal mechanical occupation number \bar{n} , and bath occupation number \bar{n}_B .

Figs. 3a and 3b show D_5 and S_3 , respectively, as functions of the experimentally controlled phase ϕ , and the optomechanical coupling μ . We have chosen $Q = 10^5$, $\bar{n}_B = 500$, and $\bar{n} = 0.1$. The state $\rho_{\text{out}}^{\{1,0\}}$ has a phase periodicity of 2π in ϕ , which is reflected in the determinants. The parameter regions for which entanglement can be verified using D_5 and S_3 are indicated by the negative values and demarcated by solid black lines. For D_5 , the negative region is centred at $\phi = \{0, 2\pi\}$ while for S_3 , it is concentrated around $\phi = \pi$. We reiterate that it is the sign of the determinants, not their magnitude which indicates entanglement. Nevertheless, a more negative determinant could be more resistant to experimental errors. That is, for successful verification, the magnitude of a negative determinant should be greater than the uncertainty of the value.

To better understand the features of Figs. 3a and 3b we examine the non-Gaussianity of the state $\rho_{\text{out}}^{\{1,0\}}$ in terms of a non-Gaussian quantifier $\delta(\rho_{\text{out}}^{\{1,0\}})$. This measures the quantum relative entropy between $\rho_{\text{out}}^{\{1,0\}}$ and a Gaussian reference state ρ_G , constructed using the first and second moments of $\rho_{\text{out}}^{\{1,0\}}$. As shown in Ref. [79, 80], this measure δ can be expressed as $\delta(\rho) = S(\rho_G) - S(\rho)$, where S is the standard von Neumann entropy. Since δ is an exact measure of non-Gaussianity [81], a greater δ suggests a greater degree of non-Gaussianity, while $\delta = 0$ implies our state is exactly Gaussian. However, the measure has no upper bound (there is no maximally non-Gaussian state) so we can only comment on a state being more non-Gaussian than another.

While we do not propose an experimental way to obtain δ , the measure $\delta(\rho_{\text{out}}^{\{1,0\}})$ is shown in Fig. 4 as a function of μ and ϕ for $\bar{n} = 0.1$. For simplicity, we have computed the non-Gaussianity of the heralded state before verification has been conducted (i.e. in the absence of mechanical decoherence). As $\mu \rightarrow 0$, the state becomes more Gaussian; physically at $\mu = 0$ there is no optomechanical

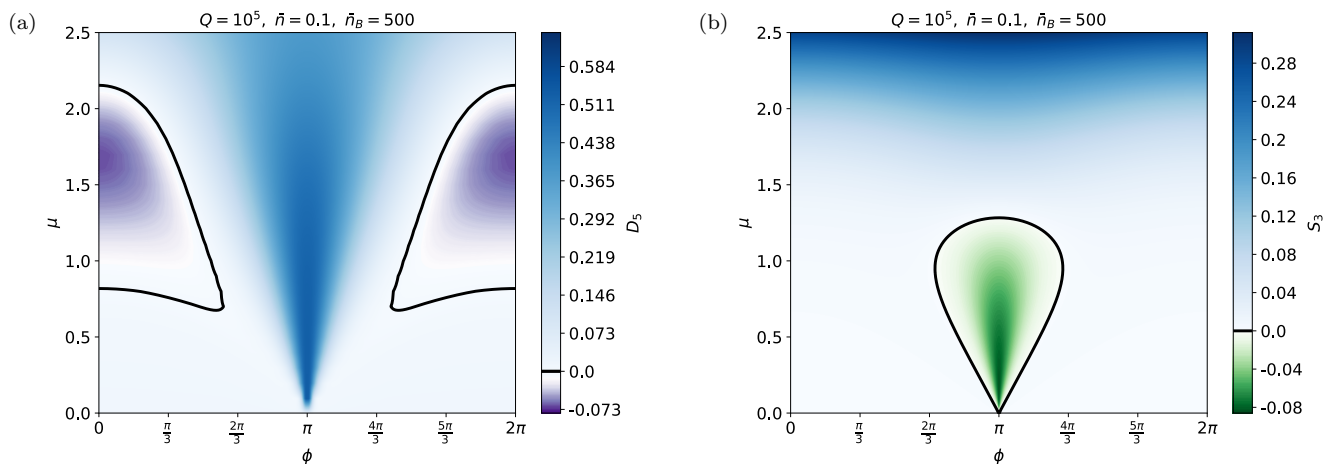


FIG. 3. Inseparability criteria outcomes as obtained via the verification method for the state $\rho_{\text{out}}^{\{1,0\}}$ produced via the parallel configuration (Fig. 1a). Plots of D_5 (a) and S_3 (b) as functions of the interferometer phase ϕ , and the optomechanical coupling strength μ . The mechanical decoherence predicted to occur while measuring the determinants (see Fig. 2) is parameterised by $Q = 10^5$, $\bar{n} = 0.1$, and $\bar{n}_B = 500$; for a summary of the experimental parameters see Table I. Both determinants are periodic with ϕ and repeat every 2π . The black line demarcates regions where determinants are negative therefore indicating regions where the state is found to be entangled. All Gaussian entangled states fall within the purple region of (a). Non-Gaussian entangled states are captured by the green region of (b) since it does not overlap with the purple region of (a).

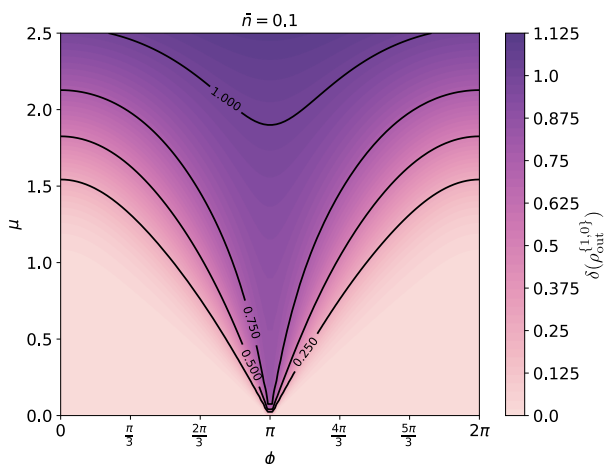


FIG. 4. Measure of non-Gaussianity computed on the mechanical state $\rho_{\text{out}}^{\{1,0\}}$ created via the entanglement scheme in Fig. 1a. The mechanical oscillators have initial thermal occupation number $\bar{n} = 0.1$. The state becomes more non-Gaussian as $\phi \rightarrow \pi$ or as μ is increased. We note that parameter regions which are more Gaussian qualitatively correlate with the negative contours in Fig. 3a. Regions which are more non-Gaussian are centred around the same phase ($\phi = \pi$) as the negative contours in Fig 3b.

interaction, therefore the state $\rho_{\text{out}}^{\{1,0\}}$ is comprised of two separable, fully Gaussian thermal states. For a given μ , the state becomes more Gaussian as $\phi \rightarrow \{0, 2\pi\}$; likewise, the negative regions of D_5 where entanglement can be verified are centred at $\phi = \{0, 2\pi\}$. This is in-line with the established notion that D_5 can detect all entanglement in bipartite Gaussian states. In contrast, for a given μ the state becomes increasingly non-Gaussian as $\phi \rightarrow \pi$. Comparing Figs. 3b and 4, we see that S_3

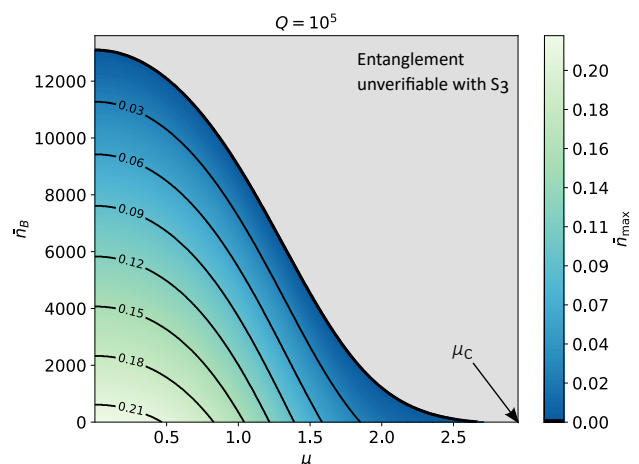


FIG. 5. Contour plot of the maximum oscillator thermal occupation \bar{n}_{max} for which S_3 can verify entanglement. This maximum is plotted with μ and \bar{n}_B for an oscillator of $Q = 10^5$. The phase in the entanglement stage is set to $\phi = \pi$. The gray region corresponds to the parameter space for which S_3 is unable to verify entanglement even at $\bar{n} = 0$. Note, for coupling strengths greater than μ_c , the scheme is unable to verify entanglement using S_3 even at $\bar{n} = \bar{n}_B = 0$ due to the decoherence present with finite γ .

performs best around the values of ϕ that correspond to higher non-Gaussianity. However, in high μ regimes, we are unable to verify entanglement with S_3 despite the state becoming more non-Gaussian as μ increases (we discuss this feature in Sec. V A).

The ability to verify entanglement is strongly dependent on the mechanical initial thermal occupation \bar{n} . This can be reduced by lowering the temperature of the oscillator using laser cooling techniques and/or cryogen-

ics. Here we determine the levels of cooling (in terms of \bar{n}) required for entanglement to be verified. We are specifically interested in non-Gaussian entanglement and therefore investigate how high we can allow \bar{n} to be while still achieving a negative S_3 . For this analysis, the phase in the entanglement stage is fixed to $\phi = \pi$ (at which point the mechanical state is most non-Gaussian). For a given μ , \bar{n}_B , and Q , the oscillators can take a range of thermal occupation numbers between $0 < \bar{n} < \bar{n}_{\max}$ over which S_3 is still negative. When $\bar{n} = \bar{n}_{\max}$, $S_3 = 0$ and we can no longer verify entanglement. The maximum mechanical occupation number \bar{n}_{\max} is shown as a function of μ and \bar{n}_B in Fig. 5 for $Q = 10^5$. As expected, in order to compensate for an increasing bath temperature one must pre-cool the oscillator more. The gray region in Fig. 5 bounded by the black line designates the values of μ and \bar{n}_B for which S_3 is not capable of verifying entanglement, even as the oscillator approaches the ground state ($\bar{n} \rightarrow 0$). We note that beyond a cut-off value of $\mu_c \approx 3.6$, S_3 cannot verify entanglement regardless of bath temperature and oscillator cooling. This does not preclude anything about the entanglement structure of the state at higher μ but would suggest S_3 is more suitable for lower μ regimes (this behaviour is further discussed in Sec. V A). In Table I, we give the values of D_5 and S_3 calculated for seven chosen parameter sets (four theoretically proposed and three taken from state-of-the-art experiments). The experiments that we consider operate in the unresolved sideband regime and so are suitable for our protocol. For the parameter sets taken from these experiments, we include both published parameters and suggested near-future improvements to the oscillator occupation number \bar{n} , and the thermal bath occupation number \bar{n}_B . Comparing the entries in the S_3 column of Table I, we see that a negative S_3 is achievable with modest amounts of additional cooling.

The final two columns of Table I give the fraction \mathcal{F} of true positive $\{1,0\}$ clicks for the corresponding experimental parameters. The ‘resolving’ photodetectors column is calculated using Eq. (12) while the ‘non-resolving’ column uses Eq. (C8). We have mentioned already that setting the amplitude of the entangling pulse to be $|\alpha| = 1$ maximises the probability P_{10} of heralding the state $\rho_{\text{out}}^{\{1,0\}}$ (Eq. (6)), therefore the main set of results in these two columns assumes $\alpha = 1$. However, in order to be confident that we have successfully heralded state $\rho_{\text{out}}^{\{1,0\}}$, we require \mathcal{F} to be as high as possible. We can experimentally tune α by attenuation, and so the values of \mathcal{F} parentheses have been optimised, having been calculated with the value of α that maximises Eqs. (12) and (C6), with all other variables in the equations kept constant.

V. DISCUSSION

A. Verification of non-Gaussian entanglement

Here we discuss the interplay of the non-Gaussian nature of the state and our ability to detect entanglement. As established in Sec. III A, the equivalence between D_5 and Simon’s criterion provides a necessary and sufficient condition for the existence of entanglement in Gaussian states. It must also be noted though that D_5 is only a sufficient criterion for non-Gaussian states. As different moments require different time delays between verification pulses they are affected by decoherence to differing degrees. If there is a high rate of decoherence across the time-scales we consider this could impede our ability to identify all Gaussian entanglement through use of D_5 . A sufficiently high quality factor, and low bath occupation \bar{n}_B , ensure that any decoherence effects are negligible, meaning that a region of state space where S_3 is negative but D_5 is positive corresponds to states which are guaranteed to be non-Gaussian. On the other hand, if decoherence does prevent us from identifying Gaussian entanglement with D_5 , then we can no longer assume merely from studying D_5 and S_3 that the state is entangled and non-Gaussian. This ambiguity could potentially be resolved using post-processing mitigation schemes that correct for the effects of noise and decoherence on measured moments [84, 85]. Within the parameter set we have explored in Figs. 3a and 3b, the region for which $S_3 < 0$ does not overlap with that where $D_5 < 0$. As the quality factor considered is large ($Q = 10^5$) we can be confident that all the states which fall in the negative (green) region of Fig. 3b are non-Gaussian, and this is confirmed by the non-Gaussianity measure shown in Fig. 4.

As discussed in Sec. IV, both the regions of high non-Gaussianity and negative S_3 are centred at $\phi = \pi$. However, we are unable to verify entanglement at higher values of μ using S_3 (Fig. 3b), despite the measure $\delta(\rho_{\text{out}}^{\{1,0\}})$ suggesting that non-Gaussianity increases with μ (Fig. 4). This is reinforced by Fig. 5 which suggests that there is a cut-off μ_c beyond which S_3 fails regardless of cooling (even when $\bar{n} = \bar{n}_B = 0$).

To aid our understanding of the behaviour of S_3 in the higher μ regime, we can examine the analytic formula for S_3 calculated for the idealised state $\rho_{\text{out}}^{\{1,0\}}$ with $\bar{n} = 0$ (defined in Eq. (5a)). Assuming no decoherence, S_3 is given by:

$$S_3 = -\frac{\mu^6 e^{-\mu^2}}{64(1 + e^{-\frac{\mu^2}{2}} \cos \phi)^3}. \quad (13)$$

Notably, this expression is negative for all choices of μ and ϕ , approaching 0 from below as $\mu \rightarrow \infty$. Also note that, Eq. (13) counter-intuitively suggests that at $\phi = \pi$, S_3 tends to $-1/8$ as $\mu \rightarrow 0$ which indicates that there is entanglement even when there is no optomechanical coupling. However, this must be considered in conjunction

TABLE I. Parameter sets of proposed and experimentally-realised values; considered for the parallel entanglement configuration with $\phi = \pi$, where ϕ is the phase in Fig. 1a. The two oscillators are characterised by the dimensionless optomechanical coupling strength μ , their quality factor Q , their initial thermal occupation number \bar{n} , and the occupation of the thermal bath \bar{n}_B . The inseparability criteria D_5 and S_3 have been calculated to incorporate the decoherence which occurs in the time elapsed between state generation and verification (see Sec. III C). We assume the following throughout: $\eta = 0.8$ (overall optical intensity efficiency), $\mathcal{D} = 10^{-8}$ (the probability of a single dark count during the detection window; assuming a dark count rate of 1 s^{-1} and a detection window of 10 ns). The fraction \mathcal{F} of true positive $\{1,0\}$ events is shown both for the case of number-resolving photodetectors (Eq. (12)) and non-resolving (Eq. (C8)). The main values of \mathcal{F} are calculated with $\alpha = 1$ (the amplitude of the injected coherent state in the entanglement stage) and the values in brackets show \mathcal{F} maximised by tuning α . (i)-(iv) are theoretically proposed parameters. Experiment-inspired parameter sets are used based on Refs [82], a micro-mechanical membrane; [40], a nanobeam oscillator; and [83], a sliced photonic-crystal structure. The rows corresponding to each of these three references are divided into two sub-rows: the first sub-row contains published mechanical parameters, in the second-row we use values for \bar{n} and \bar{n}_B based on near-future improvements (involving additional cooling techniques) of existing systems. *These \bar{n}_B values have been calculated assuming the thermal bath has been cooled to 100 mK.

Refs.	Mechanical parameters				Determinants		True positives \mathcal{F} [%]	
	μ	Q	\bar{n}	\bar{n}_B	D_5	S_3	Resolving	Non-resolving
(i)	10^{-3}	10^5	0.1	1000	0.56	-0.080	79% (84%)	79% (84%)
(ii)	10^{-2}	10^5	0.1	1000	0.56	-0.080	82% (98%)	82% (98%)
(iii)	10^{-1}	10^5	0.1	1000	0.56	-0.080	82% (> 99%)	82% (> 99%)
(iv)	10^0	10^5	0.1	1000	0.54	-0.029	82% (> 99%)	66% (> 99%)
[82]	1.69×10^{-5}	1.03×10^9	0.29	10^5	1.4	0.084	0.73% (1.6%)	0.73% (1.6%)
	1.69×10^{-5}	1.03×10^9	0.1	10^{3*}	0.51	-0.089	0.56% (1.2%)	0.56% (1.2%)
[83]	9.64×10^{-5}	7.54×10^5	5.3	2.1×10^4	3500	420	56% (57%)	56% (57%)
	9.64×10^{-5}	7.54×10^5	0.1	484^*	0.51	-0.089	15% (22%)	15% (22%)
[40]	8.44×10^{-3}	3.74×10^4	1.7×10^4	1.7×10^4	1.7×10^{17}	8.0×10^{12}	82% (> 99%)	62% (> 99%)
	8.44×10^{-3}	3.74×10^4	0.1	559^*	0.58	-0.074	82% (98%)	82% (98%)

with the heralding probability in Eq. (6) which tends to 0 as $\mu \rightarrow 0$, meaning that such a state cannot be created.

From studying this ground state behaviour (in the absence of decoherence), we see that the magnitude of S_3 decays exponentially with increasing μ . Therefore, in the regime where we consider the effects of \bar{n} and mechanical decoherence, at greater values of μ the possible negative contribution from entanglement detection is too small to compete with these effects causing S_3 to become positive. Even at $\bar{n} = \bar{n}_B = 0$ there is decoherence present due to finite γ , thus for coupling strengths greater than μ_c , the scheme is unable to verify entanglement using S_3 . Indeed, as Q is improved to values greater than 10^5 , the gray region of Fig. 5 shrinks: μ_c increases beyond 3.6, and entangled states in environments of even higher \bar{n}_B can be verified using S_3 . This analysis suggests our protocol is better suited to parameter regimes where μ is up to approximately unity, which also corresponds to what is experimentally accessible at present. The experimentally viable systems we have considered [40, 82, 83] (see Table I) are well within the range of μ where S_3 captures entanglement (Fig. 5).

B. Optical effects

The following discussion addresses the effect of optical imperfections for the coherent state input case $|\Phi\rangle_L = |\alpha\rangle_1 |0\rangle_2$ (as opposed to the single-photon input case which provides more resilience to the effects consid-

ered). Optical losses, dark counts, and the entangling pulse amplitude do not directly affect the values of the moments used to calculate D_5 and S_3 , however they do have experimental implications. For example, the entangling pulse amplitude α dictates the probability of heralding the desired mechanical state $\rho_{\text{out}}^{\{1,0\}}$, see Eq. (6). In the presence of dark counts, the fraction of false positives also depends on α , as well as on η , and \mathcal{D} . These false positive events result in mixing of the desired state with the initial state and higher photon-number contributions. This could introduce errors in the measurement of the moments for D_5 and S_3 , which can be readily mitigated by operating in a parameter regime where \mathcal{F} is close to unity ($\gtrsim 95\%$).

The rows (i) to (iv) of Table I show that \mathcal{F} is highly dependent on μ . For photon-number-resolving detectors, \mathcal{F} improves with increasing μ (keeping other experimental parameters constant). From Eq. (12) we see that as μ decreases, so does the heralding probability P_{10} (with $\phi = \pi$ in Eq. (6)), meaning that the desired state $\rho_{\text{out}}^{\{1,0\}}$ is less likely to be created. Once P_{10} is small enough that it is comparable to the dark count rate \mathcal{D} , dark counts become significant, thus reducing \mathcal{F} . By maximising Eq. (12) with respect to α , we can compensate for this reduction in \mathcal{F} , as demonstrated by the values in parentheses. For the same reasons as the photon-number-resolving case, the reduction in \mathcal{F} for small μ is also present for non-resolving photodetectors. However, non-resolving photodetectors suffer an additional drawback and thus never outperform resolving photodetectors: as μ is increased

the probability of a multi-photon interaction grows more quickly than one involving a single photon. As a non-resolving detector cannot distinguish between these and a true $\{1,0\}$ click, this reduces \mathcal{F} compared with a resolving detector (this is demonstrated in row (iv)). One can find the optimal \mathcal{F} (shown in brackets in Table I) by adjusting α in Eq. (C8) to balance the competing effects of dark counts and multi-photon events. In a similar manner to μ , increasing \bar{n} both reduces P_{10} (for $\phi = \pi$) and increases the probability of multi-photon interactions. This means that the qualitative effect of \bar{n} on \mathcal{F} can be explained by the same arguments as for μ .

VI. CONCLUSION

We have proposed a scheme to generate mechanical Schrödinger-cat states using pulsed nonlinear optomechanical interactions in conjunction with a photon-counting heralding scheme. The heralding scheme is based on an optical interferometer set-up, with a controllable phase that sets the degree of entanglement. The presence of entanglement can be confirmed in a subsequent verification stage for which we have suggested two inseparability criteria computed from moments of the mechanical state. When used together, the two criteria allow us to identify non-Gaussian entangled states. In order to obtain the moments required for the inseparability criteria, we have introduced an experimental protocol which exploits subsequent pulsed interactions and measurements. To assess the feasibility of the protocol we have included optical imperfections in the generation stage which affect the heralding success probability. Additionally, we have modelled the expected mechanical decoherence which can occur during the verification scheme.

Our findings indicate that the protocol presented here provides a realistic means of generating non-Gaussian entanglement between two mechanical oscillators. The inseparability criterion S_3 can verify entanglement in parameter regimes accessible in state-of-the-art solid-state experiments with only modest additional cooling required. While decoherence degrades the entanglement and can consequently impair our ability to verify entanglement, we have demonstrated that for realistic experimental parameters, including a low optomechanical coupling strength, our protocol is robust against decoherence.

The experimental verification scheme proposed here enables the measurement of bipartite mechanical moments of arbitrarily high order. While we have focused on extracting quadrature moments used for the two suggested inseparability criteria, any entanglement or non-classicality test that relies on measuring higher-order moments [86, 87] can be applied without making any changes to our set-up.

ACKNOWLEDGMENTS

We acknowledge useful discussions with Rufus Clarke, M. S. Kim, and B. Lez. This project was supported by the Engineering and Physical Sciences Research Council (EP/T031271/1, EP/L016524/1, and a Doctoral Prize Fellowship awarded to S.Q.), UK Research and Innovation (MR/S032924/1), and the Royal Society.

Appendix A: Verification set-up

In this Appendix we detail the key experimental steps required to calculate arbitrary mechanical moments of an entangled state, which are needed to evaluate the inseparability criteria outlined in Sec. III A. We begin by introducing the notation used to describe the moments, and then we focus on each of the two verification set-ups shown in Figs. 2 and 6. For a given mechanical moment we define the order as the sum of the exponents on the operators, e.g. the order of $\langle X_{M_1}^p P_{M_1}^q X_{M_2}^r P_{M_2}^s \rangle$ is $d = p + q + r + s$. We use the notation $\mathcal{S}(\langle X_{M_1}^p P_{M_1}^q X_{M_2}^r P_{M_2}^s \rangle)$ to denote the sum of all possible permutations of p lots of X_{M_1} -operators, q lots of P_{M_1} -operators etc., taking into account the fact that operators from different oscillators commute. For example, $\mathcal{S}(\langle X_{M_1}^2 P_{M_1} X_{M_2} \rangle) = \langle X_{M_1}^2 P_{M_1} X_{M_2} \rangle + \langle X_{M_1} P_{M_1} X_{M_1} X_{M_2} \rangle + \langle P_{M_1} X_{M_1}^2 X_{M_2} \rangle$. Knowing the value of $\mathcal{S}(\langle X_{M_1}^2 P_{M_1} X_{M_2} \rangle)$ and the lower-order moment $\langle X_{M_1} X_{M_2} \rangle$ is sufficient to gain access to $\langle X_{M_1}^2 P_{M_1} X_{M_2} \rangle$, $\langle X_{M_1} P_{M_1} X_{M_1} X_{M_2} \rangle$, and $\langle P_{M_1} X_{M_1}^2 X_{M_2} \rangle$ individually as these can be found via the commutation relation $[X_{M_i}, P_{M_j}] = i\delta_{ij}$. For example, if our desired moment is $\langle X_{M_1}^2 P_{M_1} X_{M_2} \rangle$, then $\langle X_{M_1}^2 P_{M_1} X_{M_2} \rangle = \mathcal{S}(\langle X_{M_1}^2 P_{M_1} X_{M_2} \rangle)/3 + i\langle X_{M_1} X_{M_2} \rangle$. Hence any desired moment – composed of a sequence of mechanical quadrature operators $\langle X_{M_1}^p X_{M_2}^q X_{M_2}^r X_{M_2}^s \rangle$ – can be written as the sum over the moments of all the distinct permutations of those operators $\mathcal{S}(\langle X_{M_1}^p X_{M_2}^q X_{M_2}^r X_{M_2}^s \rangle)$, plus lower-order moments (which as we shall see are already known due to the iterative nature of the procedure). This iterative procedure involves finding the moments of all the permutations of sequences of operators belonging to order d (i.e. finding values for all possible sums \mathcal{S} of order d , and consequently individual moments) before being able to unlock moments of order $d + 1$. The method prescribed can be used to find a moment with arbitrarily large d .

1. Parallel set-up

Here we will outline the key experimental steps necessary for the entanglement verification (using the set-up in Fig. 2) of a mechanical state created by the parallel set-up in Fig. 1a. We will first demonstrate that any arbitrary moment of the form $\langle X_{M_1}^p P_{M_1}^q X_{M_2}^r P_{M_2}^s \rangle$ can be calculated using our scheme. Then we will show that for

some lower-order moments, which appear in the subdeterminants of D_5 and S_3 , a simpler sequence of verification pulses can be used.

a. Generalised scheme

First, let us consider the case where our desired moment is contained within the expression $\mathcal{S}(\langle X_{M_1}^p P_{M_1}^q X_{M_2}^r P_{M_2}^s \rangle)$. The entangled mechanical state $\rho_{\text{out}}^{\{1,0\}}$ is generated following a $\{1,0\}$ click (see Fig. 1a). As discussed in the main text, this mechanical state depends on the phase ϕ in the interferometer and so this phase is kept fixed throughout the verification of the state. For generality, we have included ϕ in our expressions but it has no relevance in the verification scheme. All other phases ζ_l (where $l = 1, 2, 3, 4$) are controllable phases. After the state has been created, a verification pulse is then sent into oscillator 1 at time $\tau = 0$ followed by a second at $\tau = \pi/(2\omega_M)$. Each pulse interacts sequentially with the mechanical oscillator, and the phase quadratures of the verification pulses transform according to Eq. (9b). These verification pulses have a different wavelength to the entangling pulse to operate in

the linearized regime and so spectral filters ensure that after the optomechanical interaction all the verification pulses are diverted away from the photodetectors in Fig. 2. The first pulse follows path 1a and is held in a delay line for $\tau = \pi/(2\omega_M)$ while a switch ensures the second, later pulse is directed along 1b and thereby receives an additional phase shift ζ_1 . The two pulses are both incident at the first beam splitter simultaneously, which allows us to measure moments comprised of both position and momentum quadratures. Similarly, two verification pulses are also sent into oscillator 2 at time $\tau = 0$ and $\tau = \pi/(2\omega_M)$. After the optomechanical interaction with oscillator 2, with the aid of a spectral filter, the first pulse follows path 2a and is held in a delay line while the second, later pulse travels along 2b and experiences a phase shift of ζ_2 at the beam splitter. The light from each oscillator is then combined at two further beam splitters as depicted in Fig. 6. There is an additional phase at each of these two beam splitters, ζ_3 and ζ_4 . After the second set of beam splitters, a homodyne measurement is performed on each of the four output modes, and the phase quadratures are measured. The phase quadratures at the 4 beam splitter ports are given by:

$$P_{L_A} = [e^{i\zeta_3}(X_{M_1} + e^{i\zeta_1}P_{M_1}) + e^{i\phi}(X_{M_2} + e^{i\zeta_2}P_{M_2})]\chi/2 + P'_{L_A} \quad (\text{A1a})$$

$$P_{L_B} = [e^{i\zeta_3}(X_{M_1} + e^{i\zeta_1}P_{M_1}) - e^{i\phi}(X_{M_2} + e^{i\zeta_2}P_{M_2})]\chi/2 + P'_{L_B} \quad (\text{A1b})$$

$$P_{L_C} = [X_{M_1} - e^{i\zeta_1}P_{M_1} - e^{i(\phi+\zeta_4)}(X_{M_2} + e^{i\zeta_2}P_{M_2})]\chi/2 + P'_{L_C} \quad (\text{A1c})$$

$$P_{L_D} = [X_{M_1} - e^{i\zeta_1}P_{M_1} + e^{i(\phi+\zeta_4)}(X_{M_2} - e^{i\zeta_2}P_{M_2})]\chi/2 + P'_{L_D} . \quad (\text{A1d})$$

Here, P'_{L_k} (where $k = \{A, B, C, D\}$) can be understood as the momentum quadrature of the pulse in the absence of the oscillators, and commutes with all mechanical quadrature operators. The momentum quadratures $P'_{L_k} \propto P_{L_{\text{in}}}$; for example, the topmost output in Figure 2 has $P'_{L_A} = (e^{i\zeta_3}(1+e^{i\zeta_1})+e^{i\phi}(1+e^{i\zeta_2}))P_{L_{\text{in}}}/2$. In the main text we assumed $P_{L_{\text{in}}}$ has vacuum noise statistics, however here we generalise the expressions and assume only that all 4 verification pulses have identical initial statistics, and that their momentum quadratures after each optomechanical interaction are described by Eq. (9b).

The process of creating the entangled states, followed by sending in these four pulses of light and performing a homodyne measurement of the four outputs to measure the momentum quadratures (A1a)-(A1d) is repeated over many runs with a fixed set of phases $\{\zeta_1, \zeta_2, \zeta_3, \zeta_4\}$. This allows us to build up a histogram for each of the light quadratures in Eqs. (A1a)-(A1d). From these distributions we can extract increasing orders of moments. For example, considering Eq. (A1a) which describes the topmost output in Fig. 2, the d^{th} order moment of the optical momentum quadrature can be expanded in terms of mechanical quadratures and P'_{L_A} :

$$\langle P_{L_A}^d \rangle = (1/2)^d \sum_{j=0}^d \binom{d}{j} \langle [e^{i\zeta_3}(X_{M_1} + e^{i\zeta_1}P_{M_1}) + e^{i\phi}(X_{M_2} + e^{i\zeta_2}P_{M_2})]^j \rangle (\chi/2)^j \langle (P'_{L_A})^{j-d} \rangle , \quad (\text{A2})$$

where we have used the fact that P'_{L_A} commutes with the

mechanical quadratures. The value of $\langle P_{L_A}^d \rangle$ is calculated

from the frequency distribution of P_{L_A} . The process also assumes we know χ accurately and have already obtained full statistics on $P_{L_{in}}$ and therefore P'_{L_A} in an initial calibration stage (we discuss this in Sec. A 1 c). The remaining terms in the sum are quadrature moments of order $j = 1, \dots, d$. However, the iterative nature of the process means we have already calculated $\langle P_{L_A}^{d-1} \rangle$ and so all mechanical moments up to order $j = d - 1$ are known. Therefore, the only unknown moments in the expansion (A2) are contained in the d^{th} order term:

$$\begin{aligned} & \langle [e^{i\zeta_3}(X_{M_1} + e^{i\zeta_1}P_{M_1}) + e^{i\phi}(X_{M_2} + e^{i\zeta_2}P_{M_2})]^d \rangle = \dots \\ & + e^{ip\zeta_3 + iq(\zeta_1 + \zeta_3) + ir\phi + is(\zeta_2 + \phi)} \mathcal{S}(\langle X_{M_1}^p P_{M_1}^q X_{M_2}^r P_{M_2}^s \rangle) \\ & + \dots, \end{aligned} \quad (\text{A3})$$

where $\mathcal{S}(\langle X_{M_1}^p P_{M_1}^q X_{M_2}^r P_{M_2}^s \rangle)$ is the term we are trying to calculate. However, the other terms in the sum Eq. (A3) are of the form $\mathcal{S}(\langle X_{M_1}^{\tilde{p}} P_{M_1}^{\tilde{q}} X_{M_2}^{\tilde{r}} P_{M_2}^{\tilde{s}} \rangle)$, with $\tilde{p} + \tilde{q} + \tilde{r} + \tilde{s} = d$ and $\{\tilde{p}, \tilde{q}, \tilde{r}, \tilde{s}\} \neq \{p, q, r, s\}$. The coefficients of the terms $\mathcal{S}(\langle X_{M_1}^{\tilde{p}} P_{M_1}^{\tilde{q}} X_{M_2}^{\tilde{r}} P_{M_2}^{\tilde{s}} \rangle)$ are dictated by the combination of phases chosen $\{\zeta_1, \zeta_2, \zeta_3, \zeta_4\}$. Therefore, we repeat the entire process numerous times with a different set of phases until we obtain the sufficient number of linearly independent equations required to solve for the term $\mathcal{S}(\langle X_{M_1}^p P_{M_1}^q X_{M_2}^r P_{M_2}^s \rangle)$. We reiterate that knowledge of the value of $\mathcal{S}(\langle X_{M_1}^p P_{M_1}^q X_{M_2}^r P_{M_2}^s \rangle)$ is sufficient to calculate the moment of interest. Due to the 4 distinct beam splitter outputs, for a given set of phases $\{\zeta_1, \zeta_2, \zeta_3, \zeta_4\}$, we in fact have access to four linearly independent equations by applying the same analysis to equations (A1b)-(A1d). This reduces the number of distinct sets of phases required by a factor of 4.

b. Special cases

We will now discuss some special cases of moments that require fewer than 4 verification pulses per run. In fact, all of the moments in the subdeterminants of D_5 and S_3 fall under this category except $\langle b_1^\dagger b_1 b_2^\dagger b_2 \rangle$ for which we must use the generalised scheme. For single-mode moments $\langle X_{M_i}^d(\theta) \rangle$, we require a single verification pulse sent into the i^{th} oscillator at time $\tau = \theta/\omega_M$, where $\theta = \{0, \pi/2\}$ (no verification pulses are sent to the j^{th} oscillator, where $j \neq i$). The entangled state $\rho_{\text{out}}^{\{1,0\}}$ is first created in the usual way (see Fig. 1a). For the verification stage, the switches are position 1b and 2b since no delay lines are required. All optical phases ζ_l are set to 0. Sending in the verification pulse at time $\tau = 0$ will allow us to find $\langle X_{M_i}^d \rangle$ while sending in the pulse at time $\tau = \pi/(2\omega_M)$ will give us $\langle P_{M_i}^d \rangle$. The optical momentum quadratures are measured at each of the four beam splitter outputs, for example $P_{L_A}(\theta) = \eta_V(P_{L_{in}} + \chi X_{M_i}(\theta)) + \sqrt{1 - \eta_V}(1 + \sqrt{\eta_V})P_V$, where the vacuum noise P_V has been included from each beam splitter interaction (each beam splitter transmits

$\sqrt{\eta_V}$ of the pulse, and each mode passes through two beam splitters). We build up a frequency distribution for $P_{L_k}(\theta)$ and find all moments up to order d . Rearranging the equation for $\langle P_{L_A}^d(\theta) \rangle$ gives:

$$\begin{aligned} \langle X_{M_i}^d(\theta) \rangle &= (\eta_V \chi)^{-d} [\langle P_{L_A}^d(\theta) \rangle \\ &- \sum_{j=0}^{d-1} \binom{d}{j} (\eta_V \chi)^j \langle X_{M_i}^j(\theta) \rangle \langle (P_{L_A}')^{d-j} \rangle], \end{aligned} \quad (\text{A4})$$

where $P_{L_A}' = \eta_V P_{L_{in}} + \sqrt{1 - \eta_V}(1 + \sqrt{\eta_V})P_V$. Again, this calculation must be done in an iterative way starting with $d = 1$ (hence all the moments $\langle X_{M_i}^j(\theta) \rangle$, where $j < d$, are presumed to be already known).

For moments of the same oscillator $\langle X_{M_i}^p P_{M_i}^q \rangle$, after creating the entangled state $\rho_{\text{out}}^{\{1,0\}}$ in the usual manner, the switches are moved to position 1a for $i = 1$ (or position 2a for $i = 2$). Two pulses are sent into the i^{th} oscillator, one at time $\tau = 0$ followed by one at $\tau = \pi/(2\omega_M)$ (no pulses are sent to the j^{th} oscillator). The first pulse is held in a delay line with the switch in position 1a (or 2a). The second, later pulse follows path 1b (or 2b), experiences a ζ_i phase shift, and coincides with the first pulse at the beam splitter. All other phases can be neglected: $\zeta_j = \zeta_3 = \zeta_4 = 0$. For moments like $\langle X_{M_1}^p(\theta_1) X_{M_2}^q(\theta_2) \rangle$ one pulse is sent to oscillator 1 at time $\tau = \theta_1/\omega_M$ and a second pulse is sent to oscillator 2 at $\tau = \theta_2/\omega_M$. The phases $\zeta_1 = \zeta_2 = 0$, but the set $\{\zeta_3, \zeta_4\}$ must be varied. Finally, for a moment such as $\langle X_{M_i}^p(\theta_i) X_{M_j}^q P_{M_j}^r \rangle$, one pulse is sent into the i^{th} oscillator at $\tau = \theta_i/\omega_M$ and two pulses are sent into the j^{th} oscillator at time $\tau = 0$ and $\tau = \pi/(2\omega_M)$. All four phases in the set $\{\zeta_1, \zeta_2, \zeta_3, \zeta_4\}$ must be varied. With all these special cases, the phase quadratures P_{L_k} are measured over many runs in order to construct a histogram for given set of phases $\{\zeta_1, \zeta_2, \zeta_3, \zeta_4\}$. From the histogram all the moments up to $\langle P_{L_k}^d \rangle$ are calculated. The phases within the set are then varied (and we repeat previous step of homodyning over many runs to construct a histogram) until we have a sufficient number of linearly independent equations to solve for the term of interest. The mathematics of solving the equations is the same as the general case of $\mathcal{S}(\langle X_{M_1}^p P_{M_1}^q X_{M_2}^r P_{M_2}^s \rangle)$ and has been examined in detail in Sec. A 1.

c. Calibration

We have assumed throughout Secs. A 1 a and A 1 b that we already know the full statistics of P'_{L_k} where $k = \{A, B, C, D\}$ via a calibration step. This is an important first stage in order to accurately eliminate initial pulse moments from equations such as (A2). In the absence of any oscillators, we have that $P_{L_k} = P'_{L_k}$. Therefore, still using the optical set-up of Fig. 2, we send in the verification pulses which we would normally use to

obtain a specific moment but in the absence of any optomechanical oscillators (the experimental set-up would need to be adapted further from Fig. 2 in order to bypass the oscillators). For example, if we are using the generalised regime we would send in 4 verification pulses, 2 in each arm and time $\tau = 0$ and $\tau = \pi/(2\omega_M)$. The phases ζ_i are set to whichever set of phases $\{\zeta_1, \zeta_2, \zeta_3, \zeta_4\}$ we are intending on using for that particular run. Measuring the quadratures P_{L_k} many times to build up a frequency distribution will allow us to extract $\langle P_{L_k}^d \rangle$ for a given set of ζ_i phases.

Another assumption in the verification protocol is precise knowledge of χ , which appears in Eq. (9b) and is the interaction strength between the verification pulses and the mechanical system. One can measure χ precisely in a calibration stage which is separate from the entangling and verification steps. This involves sending pulses of light towards a mechanical state that is in thermal equilibrium and then phase-homodyning the output light. Knowledge of the statistics of the input pulses and the bath temperature allows a value for χ to be extracted from the histograms accumulated over many phase-homodyne measurements.

2. Series set-up

Our proposed set-up to verify the type of entanglement produced when the two oscillators are in series with each other is displayed in Fig. 6. In this scheme, we integrate the verification apparatus into the entanglement set-up of Fig. 1b. The mathematical method is identical to the prescribed method for the parallel set-up in Appendix A1. Sending in up to two verification pulses per run and repeating numerous times allows us to build frequency distributions for P_{L_A} and P_{L_B} . From the frequency distributions, the moments $\langle P_{L_A}^j \rangle$ and $\langle P_{L_B}^j \rangle$ for $j = 1, \dots, d$ are extracted. We can expand $\langle P_{L_A}^d \rangle$ and $\langle P_{L_B}^d \rangle$ in terms of mechanical moments of order d plus lower-order moments. The process is iterative so lower-order moments are already known, leaving only moments of order d to calculate. Repeating with different sets of phases $\{\zeta_1, \zeta_2, \zeta_3\}$ gives us access to a sufficient number of linearly independent equations which can be solved to obtain values such as $\mathcal{S}(\langle X_{M_1}^p P_{M_1}^q X_{M_1}^r P_{M_2}^s \rangle)$ and consequently actual moments can be deduced.

Appendix B: Decoherence calculations

In this appendix, we outline the method used to model mechanical decoherence for the two entangled oscillators. The time-dependent solutions to the quantum Langevin

equations (10a)-(10b) are:

$$X_M(t) = e^{-\gamma t/2} [\cos(\omega_M t) + \epsilon \sin(\omega_M t)] X_M(0) + e^{-\gamma t/2} [\sin(\omega_M t) P_M(0) + \Delta X_M(t)], \quad (\text{B1a})$$

$$P_M(t) = e^{-\gamma t/2} [\cos(\omega_M t) - \epsilon \sin(\omega_M t)] P_M(0) + e^{-\gamma t/2} [-\sin(\omega_M t) X_M(0) + \Delta P_M(t)], \quad (\text{B1b})$$

where γ and ω_M are the mechanical damping rate and angular frequency, respectively; and $\epsilon = \gamma/2\omega_M$. We have assumed the optomechanical device has a high quality factor such that $Q = \omega_M/\gamma \gg 1$. The operators $\Delta X_M(t)$ and $\Delta P_M(t)$ contain random excitations entering from the thermal bath:

$$\Delta X_{M_i}(t) = \sqrt{2\gamma} \int_0^t dt' e^{\gamma t'/2} \sin(\omega_M(t-t')) \xi_i(t'), \quad (\text{B2a})$$

$$\Delta P_{M_i}(t) = \sqrt{2\gamma} \int_0^t e^{\gamma t'/2} \xi_i(t') \times [\cos(\omega_M(t-t')) - \epsilon \sin(\omega_M(t-t'))] \quad (\text{B2b})$$

where ξ_i is the Brownian force on the i^{th} oscillators whose properties are captured in Eqs. (11a) and (11b).

Since the optomechanical interaction is governed by Eq. (9b), the X_M quadrature of a particular oscillator is imprinted on the verification pulse, and so we only make use of Eq. (B1a). For example, the moment $\langle P_{M_i} \rangle$ is measured at a time that has allowed the X_{M_i} quadrature to evolve by a quarter of a mechanical oscillation (via the use of a delay line). However, in the presence of damping, the time which is equivalent to a quarter of an mechanical cycle is no longer $\tau = \pi/(2\omega_M)$. Instead, it takes time τ' for the X_{M_i} quadrature to evolve into the P_{M_i} quadrature, where $\tau' = \arctan(-\epsilon^{-1}) + \pi/\omega_M$. In the limit that $\gamma \rightarrow 0$ then $\tau' \rightarrow \pi/(2\omega_M)$ as is expected in the absence of damping. Based on our proposed verification scheme, the value which is measured is in fact $\langle P_{M_i} \rangle = \langle P_{M_i}(0) \rangle e^{-\gamma\tau'/2} \sin(\omega_M\sigma\tau')/\sigma$, where $\langle P_{M_i}(0) \rangle$ is the expectation of the initial momentum quadrature at the time of state generation. The excitations from the bath via the Brownian force appear in second order terms like $\langle P_{M_i}^2 \rangle$. This decoherence has been taken into account for all the matrix elements in D_5 and S_3 throughout the results presented in Figs. 3a, 3b, 5, and Table I.

Appendix C: Optical losses, detector inefficiencies and resolution

In this Appendix we examine how experimental imperfections can affect the success with which we herald our desired mechanical state. We can model optical losses and detector inefficiencies which are present during the state generation stage by introducing loss-model beam splitters with intensity transmission η in the lower and

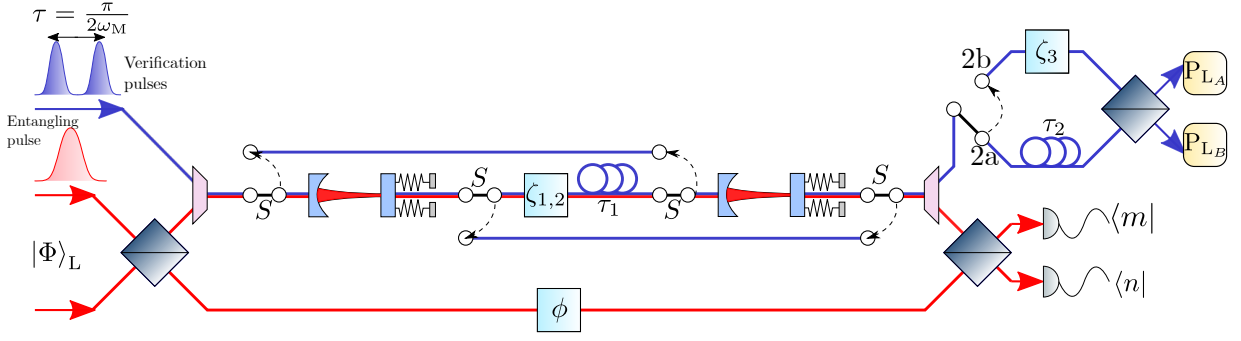


FIG. 6. Proposed verification scheme to measure mechanical moments of a state produced via the series set-up. The first stage is to create the entangled state $\rho_{\text{out}}^{\{1,0\}}$ shown by the red path on the diagram; all the switches labelled S are positioned accordingly. After a click event of $\{1,0\}$, verification pulses (which have a different wavelength) can follow different paths to that of the entangling pulse. In order to calculate a moment which appears in the sum $S(\langle X_{M_1}^P P_{M_1}^Q, X_{M_2}^R P_{M_2}^S \rangle)$ we send up to two verification pulses per run into the upper arm of the apparatus. The delay line τ_1 is useful if we wish to allow the second oscillator to freely evolve relative to the first oscillator. The switches S allow us to bypass an oscillator in order to get a single-mode mechanical moment. τ_2 allows us to delay the first verification pulse so that the two verification pulses are incident on the final beam splitter coincidentally. The other features of the set-up serve the same purpose as they do in Fig. 2.

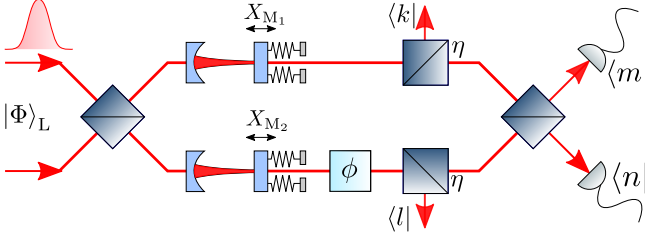


FIG. 7. Two beam splitters are introduced into the state generation optical set-up in order to model optical losses and detector inefficiencies (cf. Fig. 1a). The beam splitters have intensity transmission η , and couple the entangling pulse with the environment (which is described by vacuum states). In our formalism, k and l photons are lost to the environment in the upper and lower arms, respectively; m and n photons are measured by the photodetectors. When $|\Phi\rangle_L$ is a coherent state it is possible that more than one photon interacts with the two oscillators but the photodetectors measure $\{1,0\}$.

upper arms of the interferometer as shown in Fig. 7, such that when $\eta = 1$ there are no optical losses and the detectors are perfectly efficient. We introduce a_3 and a_4 as the annihilation operators of modes of the environment to which entangling pulse couples to at these additional beam splitters. At optical frequencies we can assume that the initial environment mode is well described by the vacuum state. The full measurement operator for the parallel configuration with an injected coherent state is given by:

$$\Upsilon_{mnkl} = \langle m|_1 \langle n|_2 \langle k|_3 \langle l|_4 U_{12} U_{24} U_{13} \\ \times e^{i\mu a_1^\dagger a_1 X_{M_1}} e^{i\mu a_2^\dagger a_2 X_{M_2} + i a_2^\dagger a_2 \phi} U_{12} \\ \times |\alpha\rangle_1 |0\rangle_2 |0\rangle_3 |0\rangle_4, \quad (\text{C1})$$

where U_{13} and U_{24} describe the unitary beam splitter interactions which couple modes 1 and 2 to the environ-

ment, with the subscript indicating which modes they act upon:

$$U_{13}^\dagger a_1 U_{13} = \sqrt{\eta} a_1 + \sqrt{1-\eta} a_3, \quad (\text{C2a})$$

$$U_{24}^\dagger a_2 U_{24} = \sqrt{\eta} a_2 + \sqrt{1-\eta} a_4. \quad (\text{C2b})$$

The measurement operator is then:

$$\Upsilon_{mnkl} = e^{-\frac{|\alpha|^2}{2}} \left(\frac{\sqrt{\eta}\alpha}{2} \right)^{m+n} \left(\frac{\sqrt{1-\eta}\alpha}{\sqrt{2}} \right)^{k+l} \frac{1}{\sqrt{m!n!k!l!}} \\ \times (e^{i\mu X_{M_1}} + e^{i\mu X_{M_2} + i\phi})^m (e^{i\mu X_{M_1}} - e^{i\mu X_{M_2} + i\phi})^n \\ \times e^{i\mu k X_{M_1}} e^{i\mu l X_{M_2} + i l \phi}, \quad (\text{C3})$$

and can be interpreted as losing k and l photons to the environment via each mode (either due to optical losses or detector inefficiencies) but measuring m and n photons at the detectors.

In addition to the case where $\{k, l\}$ photons are lost to the environment, we have the independent, binomial probability \mathcal{D} that a single dark count is detected during the detection window (we have assumed the probability of more than a single dark count to be negligible on this timescale). With a dark count rate of order 1 s^{-1} and a detection window of order 10 ns , we expect $\mathcal{D} \approx 10^{-8}$.

To calculate the probability of successfully heralding the desired mechanical state given a $\{1,0\}$ click, let $P_{mnkl} = \text{Tr}[\Upsilon_{mnkl} \rho_{\text{in}} \Upsilon_{mnkl}^\dagger]$, such that P_{mnkl} is the probability of losing $\{m, n, k, l\}$ photons at each of the outputs labelled accordingly in Fig. 7. The probability for resolving detectors to herald a mechanical state other than $\rho_{\text{out}}^{\{1,0\}}$, given a $\{1,0\}$ click, is:

$$P(\text{False}|\{1,0\}\text{click}) = \frac{(1-D) \sum_{kl} (P_{10kl} - P_{1000}) + \mathcal{D} \sum_{kl} P_{00kl}}{(1-D) \sum_{kl} P_{10kl} + \mathcal{D} \sum_{kl} P_{00kl}}, \quad (\text{C4})$$

where we have made use of Bayes' Theorem. The probability of heralding the correct $\rho_{\text{out}}^{\{1,0\}}$ state, given a $\{1,0\}$ detector click, is:

$$P(\text{True}|\{1,0\}\text{click}) = \frac{(1-D)P_{1000}}{(1-D)\sum_{kl}P_{10kl} + \mathcal{D}\sum_{kl}P_{00kl}}. \quad (\text{C5})$$

Let us denote the ratio of false positives (Eq. C4) to true positives (Eq. C5) as \mathcal{R} . Then the fraction of true positives we expect for a given number of $\{1,0\}$ clicks is $\mathcal{F} = 1/(1 + \mathcal{R})$ (shown in Eq. (12)).

We now consider the case where the photodetectors in the heralding stage are non-resolving (a $\{1,0\}$ click would indicate at least 1 photon has been detected in the upper detector, but there could be more photons present). Following the same analysis as above, the analogous equations are:

$$P(\text{False}|\{1,0\}\text{click}) = \frac{\sum_{m>0,kl}P_{m0kl} - P_{1000} + \mathcal{D}\sum_{kl}P_{00kl}}{\sum_{m>0,kl}P_{m0kl} + \mathcal{D}\sum_{kl}P_{00kl}}, \quad (\text{C6})$$

$$P(\text{True}|\{1,0\}\text{click}) = \frac{P_{1000}}{\sum_{m>0,kl}P_{m0kl} + \mathcal{D}\sum_{kl}P_{00kl}}. \quad (\text{C7})$$

The ratio of false positive (Eq. (C6)) to true positive events (Eq. (C7)) is again denoted as \mathcal{R} . Using $\mathcal{F} = 1/(1 + \mathcal{R})$ we can find \mathcal{F} for non-resolving detectors:

$$\mathcal{F} = \left[\frac{e^{-\eta|\alpha|^2}\mathcal{L}}{\eta P_{10}} + \frac{e^{-\eta|\alpha|^2}\mathcal{D}}{\eta P_{10}} \right]^{-1}, \quad (\text{C8})$$

where P_{10} is defined in Eq. (6) (for $|\Phi\rangle_L = |\alpha\rangle_1 |0\rangle_2$), and

$$\mathcal{L} = \sum_{m=1}^{\infty} \sum_{k=0}^{2m} \binom{2m}{k} \left(\frac{\eta|\alpha|^2}{4} \right)^m \frac{1}{m!} e^{-i(m-k)\phi} \lambda^{(m-k)^2}, \quad (\text{C9})$$

with $\lambda = e^{-\frac{\mu^2}{2}(1+\bar{n}_1+\bar{n}_2)}$. The results in the 'Non-resolving' column in Table I are calculated using Eq. (C8). When numerically computed, the sum over the m^{th} index is truncated at a sufficiently high m such that higher order terms are negligible. Physically, m corresponds to the number of photons at the detector, and since the entangling pulse is a weak coherent state with low mean photon number it is reasonable to neglect very high m .

-
- [1] A. K. Ekert, Quantum cryptography based on bell's theorem, *Phys. Rev. Lett.* **67**, 661 (1991).
 - [2] D. Gottesman and I. L. Chuang, Demonstrating the viability of universal quantum computation using teleportation and single-qubit operations, *Nature* **402**, 390-393 (1999).
 - [3] N. C. Menicucci, P. van Loock, M. Gu, C. Weedbrook, T. C. Ralph, and M. A. Nielsen, Universal quantum computation with continuous-variable cluster states, *Phys. Rev. Lett.* **97**, 110501 (2006).
 - [4] H.-J. Briegel, W. Dür, J. I. Cirac, and P. Zoller, Quantum repeaters: The role of imperfect local operations in quantum communication, *Phys. Rev. Lett.* **81**, 5932 (1998).
 - [5] S. Wehner, D. Elkouss, and R. Hanson, Quantum internet: A vision for the road ahead, *Science* **362** (2018).
 - [6] V. Giovannetti, S. Lloyd, and L. Maccone, Advances in quantum metrology, *Nature Photonics* **5**, 222 (2011).
 - [7] J. Joo, W. J. Munro, and T. P. Spiller, Quantum metrology with entangled coherent states, *Phys. Rev. Lett.* **107**, 083601 (2011).
 - [8] B. Hensen *et al.*, Loophole-free bell inequality violation using electron spins separated by 1.3 kilometres, *Nature* **526**, 682 (2015).
 - [9] L. K. Shalm *et al.*, Strong loophole-free test of local realism, *Phys. Rev. Lett.* **115**, 250402 (2015).
 - [10] M. Giustina *et al.*, Significant-loophole-free test of bell's theorem with entangled photons, *Phys. Rev. Lett.* **115**, 250401 (2015).
 - [11] M. Aspelmeyer, T. J. Kippenberg, and F. Marquardt, Cavity optomechanics, *Rev. Mod. Phys.* **86**, 1391 (2014).
 - [12] S. Mancini, V. Giovannetti, D. Vitali, and P. Tombesi, Entangling macroscopic oscillators exploiting radiation pressure, *Phys. Rev. Lett.* **88**, 120401 (2002).
 - [13] S. Pirandola, D. Vitali, P. Tombesi, and S. Lloyd, Macroscopic entanglement by entanglement swapping, *Phys. Rev. Lett.* **97**, 150403 (2006).
 - [14] Y.-D. Wang and A. A. Clerk, Reservoir-engineered entanglement in optomechanical systems, *Phys. Rev. Lett.* **110**, 253601 (2013).
 - [15] M. J. Woolley and A. A. Clerk, Two-mode squeezed states in cavity optomechanics via engineering of a single reservoir, *Phys. Rev. A* **89**, 063805 (2014).
 - [16] N. Vostrosablin, A. A. Rakhubovsky, and R. Filip, Pulsed quantum interaction between two distant mechanical oscillators, *Phys. Rev. A* **94**, 063801 (2016).
 - [17] J. Clarke, P. Sahium, K. E. Khosla, I. Pikovski, M. S. Kim, and M. R. Vanner, Generating mechanical and optomechanical entanglement via pulsed interaction and measurement, *New Journal of Physics* **22**, 063001 (2020).
 - [18] M. Brunelli, D. Malz, A. Schliesser, and A. Nunnenkamp, Stroboscopic quantum optomechanics, *Phys. Rev. Research* **2**, 023241 (2020).
 - [19] P. Neveu, J. Clarke, M. R. Vanner, and E. Verhagen, Preparation and verification of two-mode mechanical entanglement through pulsed optomechanical measurements, *New Journal of Physics* **23**, 023026 (2021).
 - [20] T. A. Palomaki, J. D. Teufel, R. W. Simmonds, and K. W. Lehnert, Entangling mechanical motion with microwave fields, *Science* **342**, 710 (2013).

- [21] C. F. Ockeloen-Korppi, E. Damskägg, J.-M. Pirkkalainen, M. Asjad, A. A. Clerk, F. Massel, M. J. Woolley, and M. A. Sillanpää, Stabilized entanglement of massive mechanical oscillators, *Nature* **556**, 478 (2018).
- [22] L. Mercier de Lépinay, C. F. Ockeloen-Korppi, M. J. Woolley, and M. A. Sillanpää, Quantum mechanics-free subsystem with mechanical oscillators, *Science* **372**, 625 (2021).
- [23] S. Kotler, G. A. Peterson, E. Shojaei, F. Lecocq, K. Cicak, A. Kwiatkowski, S. Geller, S. Glancy, E. Knill, R. W. Simmonds, J. Aumentado, and J. D. Teufel, Direct observation of deterministic macroscopic entanglement, *Science* **372**, 622 (2021).
- [24] K. Børkje, A. Nunnenkamp, and S. M. Girvin, Proposal for entangling remote micromechanical oscillators via optical measurements, *Phys. Rev. Lett.* **107**, 123601 (2011).
- [25] M. R. Vanner, M. Aspelmeyer, and M. S. Kim, Quantum state orthogonalization and a toolset for quantum optomechanical phonon control, *Phys. Rev. Lett.* **110**, 010504 (2013).
- [26] H. Flayac and V. Savona, Heralded preparation and readout of entangled phonons in a photonic crystal cavity, *Phys. Rev. Lett.* **113**, 143603 (2014).
- [27] T. J. Milburn, M. S. Kim, and M. R. Vanner, Nonclassical-state generation in macroscopic systems via hybrid discrete-continuous quantum measurements, *Phys. Rev. A* **93**, 053818 (2016).
- [28] K. C. Lee, B. J. Sussman, M. R. Sprague, P. Michelberger, K. F. Reim, J. Nunn, N. K. Langford, P. J. Bustard, D. Jaksch, and I. A. Walmsley, Macroscopic non-classical states and terahertz quantum processing in room-temperature diamond, *Nature Photonics* **6**, 41 (2012).
- [29] R. Riedinger, S. Hong, R. A. Norte, J. A. Slater, J. Shang, A. G. Krause, V. Anant, M. Aspelmeyer, and S. Gröblacher, Non-classical correlations between single photons and phonons from a mechanical oscillator, *Nature* **530**, 313 (2016).
- [30] K. A. G. Fisher, D. G. England, J.-P. W. MacLean, P. J. Bustard, K. Heshami, K. J. Resch, and B. J. Sussman, Storage of polarization-entangled thz-bandwidth photons in a diamond quantum memory, *Phys. Rev. A* **96**, 012324 (2017).
- [31] S. T. Velez, K. Seibold, N. Kipfer, M. D. Anderson, V. Sudhir, and C. Galland, Preparation and decay of a single quantum of vibration at ambient conditions, *Phys. Rev. X* **9**, 041007 (2019).
- [32] G.ENZIAN, J. J. Price, L. Freisem, J. Nunn, J. Janousek, B. C. Buchler, P. K. Lam, and M. R. Vanner, Single-phonon addition and subtraction to a mechanical thermal state, *Phys. Rev. Lett.* **126**, 033601 (2021).
- [33] R. N. Patel, T. P. McKenna, Z. Wang, J. D. Witmer, W. Jiang, R. V. Laer, C. J. Sarabalis, and A. H. Safavi-Naeini, Room-temperature mechanical resonator with a single added or subtracted phonon (2021), arXiv:2102.04017 [quant-ph].
- [34] G. Enzian, L. Freisem, J. J. Price, A. Ø. Svela, J. Clarke, B. Shajilal, J. Janousek, B. C. Buchler, P. K. Lam, and M. R. Vanner, Non-gaussian mechanical motion via single and multi-phonon subtraction from a thermal state (2021), arXiv:2103.05175 [quant-ph].
- [35] K. C. Lee *et al.*, Entangling macroscopic diamonds at room temperature, *Science* **334**, 1253 (2011).
- [36] R. Riedinger, A. Wallucks, I. Marinković, C. Löschnauer, M. Aspelmeyer, S. Hong, and S. Gröblacher, Remote quantum entanglement between two micromechanical oscillators, *Nature* **556**, 473 (2018).
- [37] B. Pepper, R. Ghobadi, E. Jeffrey, C. Simon, and D. Bouwmeester, Optomechanical superpositions via nested interferometry, *Phys. Rev. Lett.* **109**, 023601 (2012).
- [38] M. Ringbauer, T. J. Weinhold, L. A. Howard, A. G. White, and M. R. Vanner, Generation of mechanical interference fringes by multi-photon counting, *New Journal of Physics* **20**, 053042 (2018).
- [39] G. A. Brawley, M. R. Vanner, P. E. Larsen, S. Schmid, A. Boisen, and W. P. Bowen, Nonlinear optomechanical measurement of mechanical motion, *Nature Communications* **7**, 10988 (2016).
- [40] R. Leijssen, G. R. La Gala, L. Freisem, J. T. Muhonen, and E. Verhagen, Nonlinear cavity optomechanics with nanomechanical thermal fluctuations, *Nature Communications* **8**, 16024 (2017).
- [41] S. Mancini, V. I. Man'ko, and P. Tombesi, Ponderomotive control of quantum macroscopic coherence, *Phys. Rev. A* **55**, 3042 (1997).
- [42] S. Bose, K. Jacobs, and P. L. Knight, Preparation of nonclassical states in cavities with a moving mirror, *Phys. Rev. A* **56**, 4175 (1997).
- [43] P. Rabl, Photon blockade effect in optomechanical systems, *Phys. Rev. Lett.* **107**, 063601 (2011).
- [44] A. Nunnenkamp, K. Børkje, and S. M. Girvin, Single-photon optomechanics, *Phys. Rev. Lett.* **107**, 063602 (2011).
- [45] S. Qvarfort, M. R. Vanner, P. F. Barker, and D. E. Bruschi, Master-equation treatment of nonlinear optomechanical systems with optical loss, *Phys. Rev. A* **104**, 013501 (2021).
- [46] G. Vacanti, M. Paternostro, G. M. Palma, and V. Vedral, Optomechanical to mechanical entanglement transformation, *New Journal of Physics* **10**, 095014 (2008).
- [47] U. Akram, W. P. Bowen, and G. J. Milburn, Entangled mechanical cat states via conditional single photon optomechanics, *New Journal of Physics* **15**, 093007 (2013).
- [48] B. Xiong, X. Li, S.-L. Chao, Z. Yang, W.-Z. Zhang, and L. Zhou, Generation of entangled Schrödinger cat state of two macroscopic mirrors, *Opt. Express* **27**, 13547 (2019).
- [49] M. R. Vanner, I. Pikovski, G. D. Cole, M. S. Kim, Č. Brukner, K. Hammerer, G. J. Milburn, and M. Aspelmeyer, Pulsed quantum optomechanics, *PNAS* **108**, 16182 (2011).
- [50] E. Shchukin and W. Vogel, Inseparability criteria for continuous bipartite quantum states, *Phys. Rev. Lett.* **95**, 230502 (2005).
- [51] S. J. van Enk and O. Hirota, Entangled coherent states: Teleportation and decoherence, *Phys. Rev. A* **64**, 022313 (2001).
- [52] C. Wang *et al.*, A Schrödinger cat living in two boxes, *Science* **352**, 1087 (2016).
- [53] C.-W. Lee and H. Jeong, Quantification of macroscopic quantum superpositions within phase space, *Phys. Rev. Lett.* **106**, 220401 (2011).
- [54] B. Yadin and V. Vedral, General framework for quantum macroscopicity in terms of coherence, *Phys. Rev. A* **93**, 022122 (2016).
- [55] S. Bose, K. Jacobs, and P. L. Knight, Scheme to probe the decoherence of a macroscopic object, *Phys. Rev. A*

- 59**, 3204 (1999).
- [56] W. Marshall, C. Simon, R. Penrose, and D. Bouwmeester, Towards quantum superpositions of a mirror, *Physical Review Letters* **91**, 130401 (2003).
- [57] D. Kleckner, I. Pikovski, E. Jeffrey, L. Ament, E. Eliel, J. Van Den Brink, and D. Bouwmeester, Creating and verifying a quantum superposition in a micro-optomechanical system, *New Journal of Physics* **10**, 095020 (2008).
- [58] A. Bassi, K. Lochan, S. Satin, T. P. Singh, and H. Ulbricht, Models of wave-function collapse, underlying theories, and experimental tests, *Rev. Mod. Phys.* **85**, 471 (2013).
- [59] I. Pikovski, M. R. Vanner, M. Aspelmeyer, M. S. Kim, and Č. Brukner, Probing planck-scale physics with quantum optics, *Nature Physics* **8**, 393 (2012).
- [60] Z. Wang and A. H. Safavi-Naeini, Enhancing a slow and weak optomechanical nonlinearity with delayed quantum feedback, *Nature Communications* **8**, 15886 (2017).
- [61] J. Clarke and M. R. Vanner, Growing macroscopic superposition states via cavity quantum optomechanics, *Quantum Science and Technology* **4**, 014003 (2019).
- [62] M. A. Nielsen and I. L. Chuang, *Quantum computation and quantum information* (Cambridge University Press, 2010).
- [63] V. Guifré, Entanglement monotones, *Journal of Modern Optics* **47**, 355 (2000).
- [64] R. Simon, Peres-horodecki separability criterion for continuous variable systems, *Phys. Rev. Lett.* **84**, 2726 (2000).
- [65] L.-M. Duan, G. Giedke, J. I. Cirac, and P. Zoller, Inseparability criterion for continuous variable systems, *Phys. Rev. Lett.* **84**, 2722 (2000).
- [66] G. Giedke, B. Kraus, M. Lewenstein, and J. I. Cirac, Entanglement criteria for all bipartite gaussian states, *Phys. Rev. Lett.* **87**, 167904 (2001).
- [67] M. Lewenstein, B. Kraus, J. I. Cirac, and P. Horodecki, Optimization of entanglement witnesses, *Phys. Rev. A* **62**, 052310 (2000).
- [68] O. Gühne and N. Lütkenhaus, Nonlinear entanglement witnesses, *Phys. Rev. Lett.* **96**, 170502 (2006).
- [69] P. Hyllus and J. Eisert, Optimal entanglement witnesses for continuous-variable systems, *New Journal of Physics* **8**, 51 (2006).
- [70] G. Adesso and F. Illuminati, Entanglement in continuous-variable systems: recent advances and current perspectives, *Journal of Physics A: Mathematical and Theoretical* **40**, 7821 (2007).
- [71] A. Serafini, *Quantum Continuous Variables: A Primer of Theoretical Methods (1st ed.)* (CRC Press, Boca Raton, FL, 2017).
- [72] A. Peres, Separability criterion for density matrices, *Phys. Rev. Lett.* **77**, 1413 (1996).
- [73] M. Horodecki, P. Horodecki, and R. Horodecki, Separability of mixed states: necessary and sufficient conditions, *Physics Letters A* **223**, 1 (1996).
- [74] G. S. Agarwal and A. Biswas, Quantitative measures of entanglement in pair-coherent states, *Journal of Optics B: Quantum and Semiclassical Optics* **7**, 350 (2005).
- [75] M. G. Raymer, A. C. Funk, B. C. Sanders, and H. de Guise, Separability criterion for separate quantum systems, *Phys. Rev. A* **67**, 052104 (2003).
- [76] R. F. Werner and M. M. Wolf, Bound entangled gaussian states, *Phys. Rev. Lett.* **86**, 3658 (2001).
- [77] T. Opatrný, D.-G. Welsch, and W. Vogel, Homodyne detection for measuring internal quantum correlations of optical pulses, *Phys. Rev. A* **55**, 1416 (1997).
- [78] E. V. Shchukin and W. Vogel, Nonclassical moments and their measurement, *Phys. Rev. A* **72**, 043808 (2005).
- [79] M. G. Genoni, M. G. A. Paris, and K. Banaszek, Quantifying the non-gaussian character of a quantum state by quantum relative entropy, *Phys. Rev. A* **78**, 060303 (2008).
- [80] M. G. Genoni and M. G. A. Paris, Quantifying non-gaussianity for quantum information, *Phys. Rev. A* **82**, 052341 (2010).
- [81] P. Marian and T. A. Marian, Relative entropy is an exact measure of non-gaussianity, *Phys. Rev. A* **88**, 012322 (2013).
- [82] M. Rossi, D. Mason, J. Chen, Y. Tsaturyan, and A. Schliesser, Measurement-based quantum control of mechanical motion, *Nature* **563**, 53 (2018).
- [83] D. J. Wilson, V. Sudhir, N. Piro, R. Schilling, A. Ghadimi, and T. J. Kippenberg, Measurement-based control of a mechanical oscillator at its thermal decoherence rate, *Nature* **524**, 325 (2015).
- [84] Y. Li and S. C. Benjamin, Efficient variational quantum simulator incorporating active error minimization, *Phys. Rev. X* **7**, 021050 (2017).
- [85] K. Temme, S. Bravyi, and J. M. Gambetta, Error mitigation for short-depth quantum circuits, *Phys. Rev. Lett.* **119**, 180509 (2017).
- [86] S. P. Walborn, B. G. Taketani, A. Salles, F. Toscano, and R. L. de Matos Filho, Entropic entanglement criteria for continuous variables, *Phys. Rev. Lett.* **103**, 160505 (2009).
- [87] E. Shchukin, T. Richter, and W. Vogel, Nonclassicality criteria in terms of moments, *Phys. Rev. A* **71**, 011802 (2005).